The Growth and Crystallisation of Polycrystalline Heusler Alloy Thin Films

Oliver Samuel Whear

Master of Science by Research

University of York

Physics

August 2014

Abstract

Iridium is arguably the scarcest element on Earth and is currently in high demand for a number of highly technical applications. In recent years Iridium has been introduced in to the read heads of hard disk drives as well as the next generation of magnetic memory. This has led to a severe increase in the production costs of these devices because of the continuing increase in the price of Iridium. In this study the Heusler alloys Ni_2MnAl and Fe_2VAl have been investigated as part of a wider project to find materials that are suitable for replacing the antiferromagnetic Iridium based compounds used in magnetic media. The alloys were grown and crystallised in thin film form using Argon sputtering in order to replicate the type of films used in industry. The films were found to crystallise when annealed at a range of temperatures however the degree of ordering was not sufficient for an antiferromagnetic state to be observed. Doping the alloys with transition metals lowered the crystallisation temperature of the films and growth on a seed layer was found to greatly improve the film quality. This led to the observation of ferromagnetic ordering within the samples which was not suitable for the replacement of Iridium. An experimental protocol for energy dispersive X-ray spectroscopy using a scanning electron microscope was optimised for the measurement of Heusler alloys whereupon the combination of light and heavy elements was challenging to measure accurately. This is the first time that Ni_2MnAl and Fe_2VAl have been produced as polycrystalline thin films with the intention of replacing a critical material used in industry.

Contents

Contents

List of Figures

List of Tables

Acknowledgements

This thesis would have been possible without the help and support of many people in both my personal and professional life. I would like to extend my sincere gratitude to my supervisors Professor Kevin O'Grady and Dr Atsufumi Hirohata for their tuition and guidance throughout the project. I would also like to thank my fellow students in the Quantum Nanoelectronics research group for making the year so much fun. In particular I would like to thank David Lloyd for his 'special' brand of humour that can only be described as sui generis. I would also like to thanks Teodore Huminiuc for sharing several valuable discussions about the groups work on Heusler alloys within the HARFIR project.

Finally I would like to give my dearest thanks to my family. I will never be able to express how lucky I feel to have so much support and love for those dearest to me as they gave me the strength and ambition to finish this work. I have always been inspired by the generosity and strong work ethic of my father and I hope that this thesis serves as a demonstration that I am trying to follow his path.

Declaration

I declare that the work presented in this project is based purely on my own research unless otherwise stated and has not been submitted for a degree in either this or any other university.

Chapter 1: The Iridium Problem

Iridium is the scarcest element in the Earth's crust with a concentration of 4 x 10^{-4}ppm [1]. It is far rarer than Gold which has a concentration of 3 x 10^{-3}ppm [1]. The Bushveld Complex in South Africa is the main global producer of Iridium with smaller deposits in Norilsk, Russia and the Sudbury basin in Canada providing much of the remaining supply [2]. The demand for Iridium has increased dramatically in recent years. For example the demand in 2010 was approximately 10 tonnes whereas it was approximately 2 tonnes in 2009 [3]. The sudden increase in the demand for Iridium is due to number of new technological applications being developed [4] which include crucibles for production of single crystal oxides [5], spark plugs [6] and read heads in hard disks [7]. This has led to a significant increase in the price of Iridium from around $200 per ounce in 2004 to around $600 per ounce in 2014 [4] which has been caused by the global demand of around 10 tonnes outstripping the global supply of around 6 tonnes per year.

The electronics industry has been the main source of new technological applications for Iridium compounds. The use of Iridium compounds in light emitting diodes for televisions and antiferromagnets for data storage has increased the demand from 0.2 tonnes per year in 2009 to 6 tonnes per year in 2010 [4]. In order to prevent the price of future electronic devices from soaring Iridium must be substituted by cheaper materials. Iridium Manganese is an antiferromagnetic alloy that has become widely used in spin electronic devices such as hard drives and next-generation magnetic memory devices for the thermal stabilisation of data. A potential replacement of Iridium Manganese could be found in a class of ternary alloys known as Heusler alloys. There are over 3000 Heusler alloys that are predicted to exist and some are predicted to be antiferromagnetic [8]. A number of the antiferromagnetic Heusler alloys contain cheap elements such as Iron, Manganese and Aluminium. Therefore cheap antiferromagnetic Heusler alloys could be a potential replacement for Iridium Manganese in electronic devices. The use of such materials could potentially reduce the production costs of the antiferromagnetic layers in future devices by a factor of 10.

1.1 The HARFIR project

The Heusler Alloy Replacement for Iridium (HARFIR) project began in September 2013. The aim of the project is discover an antiferromagnetic Heusler alloy that does not contain the rare metal Iridium [9]. The suitability of any replacement antiferromagnetic Heusler alloys will be demonstrated in a device concept by the end of the 42-month project. Some potentially antiferromagnetic Heusler Alloys have been identified and are listed in Table 1.1. The device should show an exchange bias which is the effect of a hysteresis loop shift caused by the coupling of an antiferromagnet and a ferromagnet [10] greater than 1 kOe in thin film form with a blocking temperature greater than 300K in order to qualify with industry read head standards [9]. A number of potential antiferromagnetic Heusler alloys have been identified for the project and are listed in table 1.1. The first stage of the project was to produce a series of thin films for evaluation. The structural and magnetic properties of the materials have been characterised across a range of growth conditions. The key parameter in realising antiferromagnetic order in Heusler alloys is tuning the interplanar spacing in the lattice such that the spins in adjacent planes order antiferromagnetically [8]. The interplanar spacing can be changed in many Heusler alloy systems with variations in the composition and crystallinity of the compound [8]. Therefore the HARFIR project aims to optimise the growth conditions for a number of Heusler alloy thin films with supporting *ab initio* calculations. The remaining work in the project will focus on the fabrication of device concepts to measure fundamental properties of the materials such as their antiferromagnetic anisotropy [9].

Heusler Alloy
Fe_2VAl
Ni_2MnAl
Cr_2MnSb
Fe_2TiSi
Co_2TiAl
Mn_3Al

Table 1.1: Heusler alloys identified as being suitable for the HARFIR project [9].

There are several partners that are involved in the HARFIR project. Each member of the project provides unique a skill set of experimental or computational techniques that provide a new understanding of the properties of the selected Heusler alloys. The European team is headed at the University of York where the sputtering growth procedures of the selected Heusler alloys are optimised. The University of Bielefeld provides growth of epitaxial films. York and Bielefeld

will produce device concepts with different growth techniques in order to compare how the fabrication processes affect the properties of the devices. The University of Konstanz and the Budapest University of Technology and Economics provide *ab initio* calculations that model the electronic band structure and magnetic behaviour of the selected Heusler alloys. The Japanese team consists of the University of Tohoku and the High Energy Accelerator Research Organisation known as KEK. Tohoku produces both thin film and bulk samples for analysis in order to support and expand the experimental work conducted at York and Bielefeld. The bulk samples that are produced in Tohoku are analysed by KEK with neutron diffraction and high energy X-ray diffraction.

1.2 The growth and crystallisation of polycrystalline Heusler alloy thin films

The Heusler alloys Ni_2MnAl and Fe_2VAl were chosen for study as they were considered to be the best candidates for displaying antiferromagnetic order as discussed in Chapter 2. The aim of the work was to crystallise the Heusler alloys that could be suitable for device applications in thin film form. The magnetic properties and the physical properties of the two Heusler alloys were compared when analysed under identical conditions in order to understand how the behaviour of the films varied. The growth parameters of the thin films had to be mapped in order to optimise the quality of the thin films that were produced. The Heusler alloys were sputtered at a thickness of 100nm from powder metallurgy targets. The effect of annealing the films at temperatures up to 700^{o}C for up to 6 hours was studied in order to understand how the compounds crystallise. The composition of the samples was then adjusted in an attempt to induce antiferromagnetic ordering of the spins in the lattice following crystallisation of the films.

The quality of the films was characterised by using X-ray diffraction to determine the crystallisation of the films. The presence and relative intensities of superlattice peaks were used to determine the ordered phase of the crystals. Magnetic measurements were made in order to assess how the crystallinity of the samples affects the magnetic ordering of the films. The results were then compared with data from the literature in order to determine whether the Heusler alloys were behaving as predicted or whether artefacts being generated by the growth or annealing conditions. The composition of the thin films was measured using energy dispersive X-ray spectroscopy in a scanning electron microscope. The initial spectroscopy results found that measuring the Heusler alloys was difficult to reproduce. Therefore the experimental procedure was investigated and adapted to improve the accuracy and reproducibility of the results. The samples also underwent chemical analysis at a company called InterTek [11] in order to validate the spectroscopy measurements.

Chapter 2: Technical Background

2.1 Key magnetic principles

Heusler alloys are fascinating because their magnetic properties are tuneable by altering a wide range of physical parameters such as the chemical composition, crystal ordering and inter atomic spacing [8]. In this project both ferromagnetic and antiferromagnetic Heusler alloy thin films were studied. It is therefore important to understand the fundamental physical principles upon which these different properties are realised. In each of the Heusler alloy systems studied the magnetic properties can be explained by the exchange interaction between the atoms in the lattice. Therefore in order to communicate the behaviour of each of the Heusler alloys the key concepts of magnetism should first be addressed. This section will also discuss the electron exchange interaction between antiferromagnetic (AF) and ferromagnetic (F) layers in a thin film sample.

2.1.1 Direct exchange

Direct exchange is the interaction of the spins of two electrons associated with neighbouring atoms. It is a result of the overlapping of their quantum mechanical wave functions. In the overlapping region the electrons are indistinguishable therefore the neighbouring atoms can be said to 'exchange' electrons [12]. The energy associated with the electron exchange is given by:

$$E_{ex} = -2J_{ex}\boldsymbol{S_i}.\boldsymbol{S_j} \tag{2.1}$$

where J_{ex} is the exchange integral and $\boldsymbol{S_i}$ and $\boldsymbol{S_j}$ are the spin angular momentum vectors associated with electrons *i* and *j*. The exchange energy describes the direction and magnitude of the coupling

between spins. The sign of J_{ex} describes the alignment of the spins such that a positive sign describes parallel (ferromagnetic) coupling and a negative sign describes antiparallel (antiferromagnetic) coupling [13].

In a metal the magnetic properties are determined by the energy cost of aligning spins either parallel or antiparallel in the energy bands caused by conduction electrons near the Fermi energy (E_F). Therefore tuning the band structure of a Heusler alloy can ultimately lead to tuning its magnetic properties. The condition for ferromagnetism in a metal is defined by the Stoner criterion [14]:

$$J_{ex}(E_F)n(E_F) > 1 \tag{2.2}$$

where $n(E_F)$ is the density of electronic states at the Fermi level. Therefore, in order to engineer a ferromagnetic Heusler alloy a high density of states and exchange integral at the Fermi level is ideal. A full explanation of the direct exchange in alloys can be found in *Morrish* [15].

The extent of the overlapping of the electron wave functions leads to J_{ex} being dependent on the separation of the *d* orbitals in the localised electrons and the separation of the atoms in a material. Exchange interactions are incredibly short range ($E_{ex} \propto 1/r^6$) and as a result are highly dependent on the structure of a sample [12]. The Bethe-Slater curve shown in figure 2.1 is most commonly used to describe the variation of J_{ex} with atomic separation r_a:

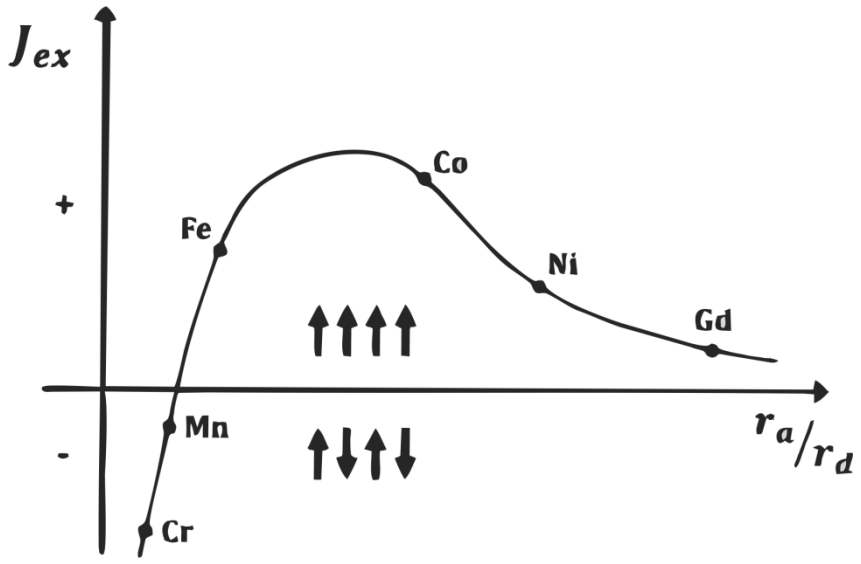

Figure 2.1: The dependence of the exchange integral *Jex* on the atomic separation r_a normalised to the electron radius in the *d* orbital r_d [12].

At large atomic separation J_{ex} becomes positive corresponding to the ferromagnetic alignment of spins. This is because at a large separation the electrons have different spacial co-ordinates but matching wave functions resulting in the parallel spin alignment being energetically favourable [14]. It is in the peak of this region the most ferromagnetic materials Iron, Cobalt and Nickel are found. At very large distances the exchange interaction becomes negligible due to the electrostatic interaction between the elections becoming asymptotic. At smaller distances J_{ex} becomes negative as antiparallel ordering becomes favourable. The Pauli Exclusion Principle dominates for distances small enough for electrons to be considered at the same point in space and therefore the spins must align antiparallel. The model correctly predicts the magnetic properties for pure elements however it must be adjusted for alloy systems. This is to account for the bonding between atoms as well as the hybridisation of orbitals and to adjust J_{ex} for the number of electrons contributing to the magnetic properties of the system. The magnetic properties of each Heusler alloy studied in this project will be reviewed in detail in section 2.3.

2.1.2 Indirect exchange mechanisms

Indirect exchange is the coupling of magnetic moments of atoms from mechanisms mediated by conduction electrons (RKKY) or non-magnetic anions (super exchange). The RKKY interaction was developed by *Ruderman and Kittel* [16], *Kasuya* [17] and *Yosida* [18] in order to explain the coupling of nuclear spins to *s*-electrons. The model has been used to explain other magnetic phenomena such as coupling between separated magnetic layers and intergranular exchange coupling in polycrystalline thin films [19]. When a magnetic impurity is placed in the lattice of a magnetic material the wave functions of the conduction electrons in the local region change. This is due to the effect of adding possible spin states in alignment with the impurity electrons [20]. The electrons in this region become part of a series of charge and spin density oscillations that contain information about the initial spin state of the impurity. Therefore magnetic atoms within range of these oscillations will couple either ferromagnetically or antiferromagnetically to each other depending on the spin density of states at their respective spatial co-ordinates.

Like direct exchange, indirect exchange coupling is highly sensitive to the distance between local moments. *Parkin et al* verified this experimentally by separating ferromagnetic (F) layers with transition metals of varying thickness [19]. The experiment showed that the nature and magnitude of the coupling was represented by the saturation field of the sample. For low distances of separation (0.5 – 1.5 nm) the F layers coupled antiferromagnetically as was demonstrated by a large saturation field (10 – 20 Oe). For larger separations the layers coupled ferromagnetically with effects observed at distances up to a range ~5 nm. The long range is

important because interactions can occur across crystal grain boundaries. This means that the grains in a system can become exchange coupled and reverse their magnetisation like a single body with a 'weak link' at the grain with the lowest magnetic energy barrier. The process of granular coupling has been well documented in granular thin film media [21]. As such, intergranular exchange is an important consideration while studying polycrystalline Heusler alloy thin films.

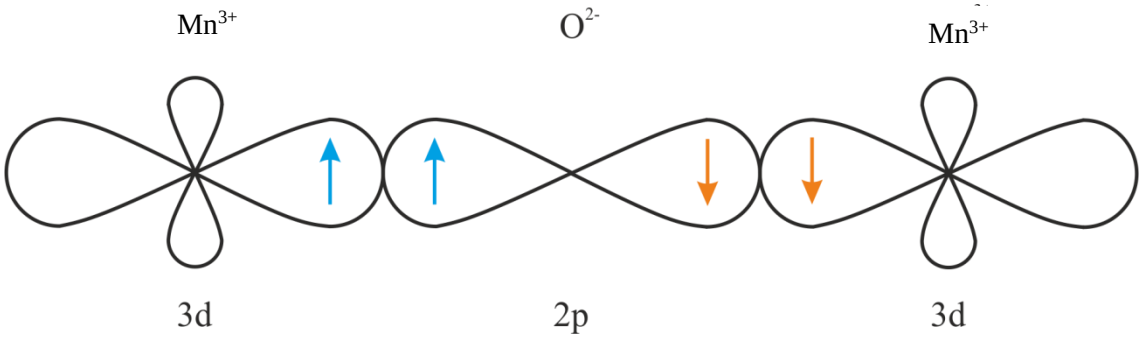

Figure 2.2: Antiferromagnetic exchange coupling in MnO

Superexchange is the mechanism by which two magnetic nearest neighbours are coupled by a mediating non-magnetic ion. The nature of the coupling is dependent on the angle between the atoms for example in MnO antiferromagnetic coupling is observed for Mn atoms being parallel to the O atoms, whereas ferromagnetic coupling is observed for Mn atoms being perpendicular to the O atoms. Figure 2.2 shows the classical example of this interaction as Manganese nearest neighbours couple antiferromagnetically due to their *d* shell electron spins coupling with an intermediary Oxygen *p*-shell electrons. *Kramers* proposed superexchange however the model was refined semi-empirically by *Goodenough* and *Kanamori* [22]. By considering the RKKY interaction for long range exchange coupling in a thin film and superexchange for the exchange coupling in unit cells it is possible to build a picture of the magnetic ordering in Heusler alloys as discussed further in section 2.2.2. Changing the interatomic spacing between neighbouring atoms can cause the exchange coupling to be reversed in order to obtain desired magnetic properties in a material. This is why the crystallisation and composition of the Heusler alloys in this work is important for the realisation of properties suitable for technological innovation.

2.1.3 Bilayer interactions in thin films

As discussed previously the RKKY interaction can lead to the coupling of adjacent grains in a thin film. The interaction can also couple grains across interfaces in thin films and is of significant technical importance as it can explain phenomena such as giant magnetoresistance for spintronics applications. Exchange bias is the coupling of a ferromagnetic and antiferromagnetic layer that ultimately leads to an increase in the magnetic energy barrier and coercivity of the ferromagnetic layer. Coupling of ferromagnetic Heusler alloys to an Iridium Manganese antiferromagnet has already been demonstrated [23]. For successful exchange bias to be observed with an antiferromagnetic Heusler alloy the layer must crystallise to favour antiferromagnetic ordering and the interface with the ferromagnetic layer must be suitable for RKKY type exchange.

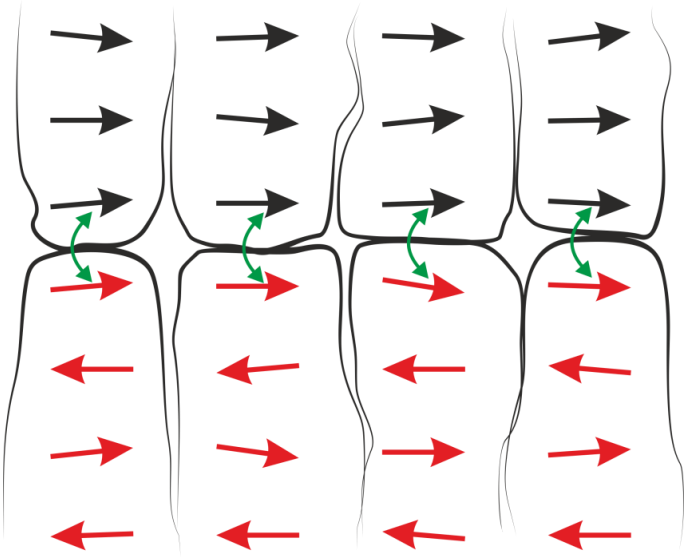

Figure 2.3: Interfacial coupling between a ferromagnet (black) and an antiferromagnet (red) in a granular thin film.

A schematic of interfacial exchange coupling is shown in figure 2.3. The spins of the antiferromagnet pin the ferromagnet which can lead to an increase in coercivity. In order for the grains to couple the physical contact of the materials at the interface must be optimised. For entirely Heusler alloy based systems the ferromagnetic and antiferromagnetic layers must have the desired magnetic ordering. This means that both layers must crystallise favourably at low enough temperatures for diffusion of the elements to not disrupt the desired magnetic properties of the bilayer. In order to surpass this challenge a range of crystallisation parameters must be mapped and optimised for individual Heusler alloys prior to growing bilayers.

2.2 Understanding Heusler alloys

Heusler alloys are a group of semiconducting or metallic materials of three elements X Y and Z with a 1:1:1 or 2:1:1 stoichiometry [8]. They have been actively researched since their discovery by Heusler in 1903 because of their range of properties [24]. These properties form several sub-classifications which can include tuneable band gap semiconductors [25], half-metallic ferromagnets with band gaps for only one spin direction [26] as well as several others [27, 28]. The properties of several Heusler alloys can be predicted by counting the number of valence shell electrons [8]. More detailed studies predict the properties of Heusler alloys based on their band structure [27]. The magnetic properties of Heusler alloys are highly sensitive to the atomic arrangement in the lattice and its degree of structural ordering [8]. Understanding the order-disorder phenomena of a Heusler alloy is critical to tuning the desired properties. For example Fe_2VAl fully ordered is ferromagnetic however $Fe_{2.5}V_{0.5}Al$ is predicted to be antiferromagnetic [29]. Therefore this section aims to detail some of the basic rules for understanding Heusler alloys to contextualise the results reported in Chapter 4.

2.2.1 Crystal ordering of Heusler alloys and the Strukturberichte notation

The order and distribution of atoms in a Heusler alloy strongly affect their electronic structure and hence their physical properties. The significance of disorder on the electronic structure can be demonstrated by TiNiSi [8]. When perfectly ordered TiNiSi has a band gap of around 0.4eV however when the lattice has a 5% site disorder the band gap is reduced to less than 0.1eV and is completely closed at 50% disordering of the lattice. Therefore if TiNiSi was used as a semiconductor in industry an extremely well-controlled production process would be required. The term disorder refers to any deviation from an idealised unit cell. However a greater level of detail is required in order to communicate exactly how the lattice is disordered. For example X elements could be occupying Y sites or there could be no ordering between the Y and Z sites in a lattice. Due to the difference between the properties such as the electronegativity and atomic radius of each element, knowledge of the subtle differences in the types of disorder are required to explain the changes in the properties of a Heusler alloy. Therefore the type of disorder associated with a Heusler alloy is described by the Strukturberichte notation as shown in figure 2.4 [8].

The Strukturberichte notation is common in the field of Heusler alloys; it is used to describe disorder based on the occupancy of different atomic sites with various elements or vacancies. In practice the Strukturberichte notation is analogous to the other common crystallographic classifications *Pearson*, prototype and space group [30]. The notation works by classifying a metallic structure by using a capital letter followed by a number and sometimes a

subscript [31]. The A-series is supposed to describe *fcc*-order in elemental structures however it is used in X_2YZ Heusler alloys to describe a system whereby an ordered lattice that is present that is occupied by random elements within the alloy composition. The B-series is used to describe binary systems for example 'B2' describes the CsCl structure in prototype notation. In X_2YZ Heusler alloys it is used to describe the situation when the lattice is formed of two sublattices. Finally the L-series is used to describe alloy structures whereupon $L2_1$ describes a fully ordered X_2YZ alloy structure. The Strukturberichte notation is ideal for this work as samples can be identified from having the minimum A2-type disorder to the perfect $L2_1$-type order. The notation forms a convenient system for discussing how the crystal structure of the samples changes under specific growth conditions. Figure 2.4 is a schematic of the three Strukturberichte classifications used to describe the experimental results found in Chapter 4. It should be noted that the classifications shown are displayed with unit-cells to reflect how the structures are commonly used to describe Heusler alloys. For example where B2 would normally describe a CsCl structure of two elements, in Figure 2.4 it is describing two ordered sublattices occupied by element X in one sublattice and elements Y and Z in the second sublattice. Therefore Strukturberichte is used in the rest of this work to describe the structures shown in Figure 2.4 which are discussed further below.

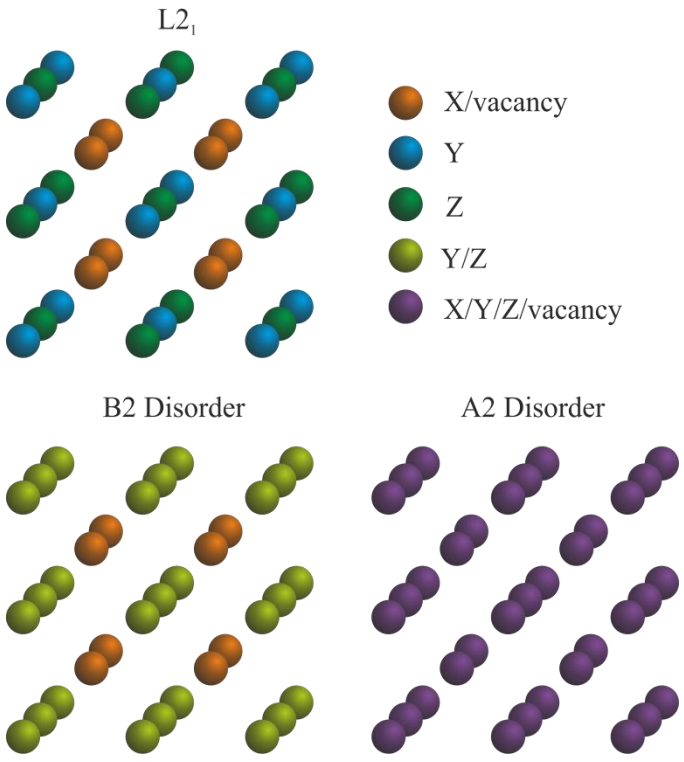

Figure 2.4: A diagram of disorder in a X_2YZ Heusler alloy lattice based on the occupation of sites by specific elements as described by the Strukturberichte notation.

The types of disorder shown in figure 2.4 are considered the most important for this work because they are associated with the different types of magnetic ordering in the Heusler alloys chosen. The $L2_1$ structure is perfectly ordered by definition whereupon the X, Y and Z unit cells form an interlocking *fcc*-based supercell. The B2 disorder describes the situation whereupon the X element has formed ordered cells within the lattice however the Y and Z elements occupy adjacent sites at random. The A2 disorder describes the situation whereupon a Heusler alloy has formed a lattice however the elements are randomly distributed amongst the lattice sites. The films grown in this work are typically deposited in an A2 matrix. *Fleet et al* [32] observed the crystallisation of Co_2FeSi from the A2 to the $L2_1$ phase using transmission electron microscopy. Highly ordered nanocrystals were observed growing from the deposited matrix in a layer-by-layer crystallisation process. The work also indicated that there could be preferential crystal growth along a specific axis. A great deal of time must be invested in studying materials using transition electron microscopy therefore a more efficient measurement technique was required to screen samples.

The most common method for determining the structure of Heusler alloys is X-ray diffraction [8]. This is because the different ordering structures exhibit different reflection profiles based on the relative intensities of the planar reflections as shown in table 2.1. The absence of peaks can be used as a strong indication of the degree of ordering with more peaks indicating a higher degree of crystallinity. The ordered $L2_1$ structure is identified by the presence of the (111) and (200) *fcc*-typical reflections with respect to the (220) reflection. However for compounds containing elements of similar atomic number the (111) and (200) reflections can be below 1% of the intensity of the (220) reflection [8]. Therefore a simulation of the expected sample response is valuable for the interpretation of X-ray data. The elements comprising the Heusler alloys in this project had a sufficient difference in mass for there to be enough intensity in the reflections to justify X-ray diffraction as a primary measurement. The different types of disorder in Heusler alloys have characteristic X-ray diffraction profiles [8]. Therefore the phase of the material could be identified by the relative intensities of the diffraction peaks observed. Table 2.1 lists the reflections and relative intensities used to identify the different types of disorder. Figure 2.5 is a simulation of the X-ray profile of a perfectly ordered $L2_1$ structure. This phase and the B2 and A2 were identifiable because the (220) intensities were at least 10^3 counts per second (cps) which meant minor peak intensities were of the order of 10^2 cps which exceeded a typical noise floor of 10cps in the X-ray diffractometer.

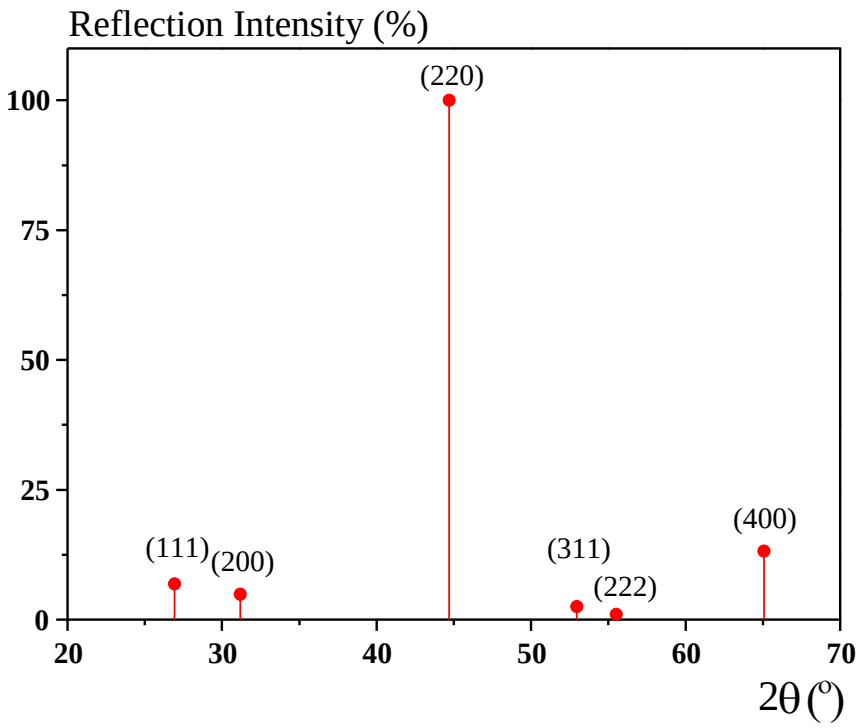

Figure 2.5: The X-ray diffraction profile and schematic of $L2_1$ ordered Fe_2VAl calculated using the CaRIne crystallography software package.

The CaRIne crystallography software package [33] was used to calculate the diffraction profile shown in figure 2.5. In order to calculate the intensities of the peaks CaRIne applies Bragg diffraction to a unit cell designed by the user. Each plane is described by Miller indices (*hkl*) which are used to calculate the structure factor F_s:

$$F_s = \sum_{n=1}^{N} f_n . f_{occ} . e^{2\pi i(h.x_n + k.y_n + l.z_n)} \tag{2.3}$$

where f_n is the atomic scattering factor for X-rays, x_n y_n and z_n are the atomic coordinates for the n^{th} atom and f_{occ} is the occupation factor of the site ($0 \leq f_{occ} \leq 1$). The occupation factor is addition of the Lorentz and polarisation factors to account for unpolarised incident X-rays and the change of the diffraction geometry as the incident X-rays are swept across the diffraction angle θ. The software uses the following equations to calculate these factors:

$$f_{Lorentz} = 1/4 . sin^2\theta . cos\theta, \tag{2.4}$$

$$f_{polarisation} = \frac{1}{2} . (1 + cos^2\theta). \tag{2.5}$$

The software also allows the user to add a temperature factor f_T to describe the Debye Wallor attenuation of X-ray scattering due to thermal motion in the sample. Once the structure factor has been calculated CaRIne then calculates the intensity *I* of X-ray diffraction for a given diffraction angle:

$$I = \|F_s\|.\left(\frac{1+cos^2 2\theta}{sin^2\theta.cos\theta}\right).e^{-2f_t\left(\frac{sin\theta}{\lambda}\right)^2}.p.V^{-1} \quad (2.6)$$

where *p* is the X-ray polarisation and *V* is the volume of the unit cell. The intensities of the respective peaks are around 2% different to the values quoted in table 2.1 because the Heusler alloys used in the calculations have different lattice parameters resulting in a different volume of the unit cell.

Structure	(111)	(200)	(220)	(311)	(222)	(444)
$L2_1$	4.30	4.67	100	2.01	1.30	16.46
B2	-	4.67	100	-	1.30	16.46
A2	-	-	100	-	-	16.58

Table 2.1: The relative X-ray diffraction intensities of Co_2MnSi for different structures [34].

2.2.2. Magnetic ordering of Heusler alloys

The Heusler alloy family contains a diverse spectrum of magnetic phenomena. A wide range of properties have been predicted or observed experimentally these include: ferromagnetism, antiferromagnetism, Pauli paramagnetism and heavy-fermionic behaviour [35, 36]. The majority of $L2_1$ ordered Heusler alloy thin films are ferromagnetic and saturate at low applied fields (100Oe). This is often due to ferromagnetic coupling between the superlattice and sublattices as demonstrated in figure 2.6. Co_2FeSi is commonly used as it has the highest Curie temperature (T_c = 1100K [37]) and moment (m = 5.97 μ_B/atom [38]) of ferromagnetic Heusler alloys. The ferromagnetism of Heusler alloys is widely studied due to the half-metallic density of spin states predicted for several compounds [8, 39]. This means that a band gap is present for one spin direction only leading to a very high level of spin polarisation being predicted [39].

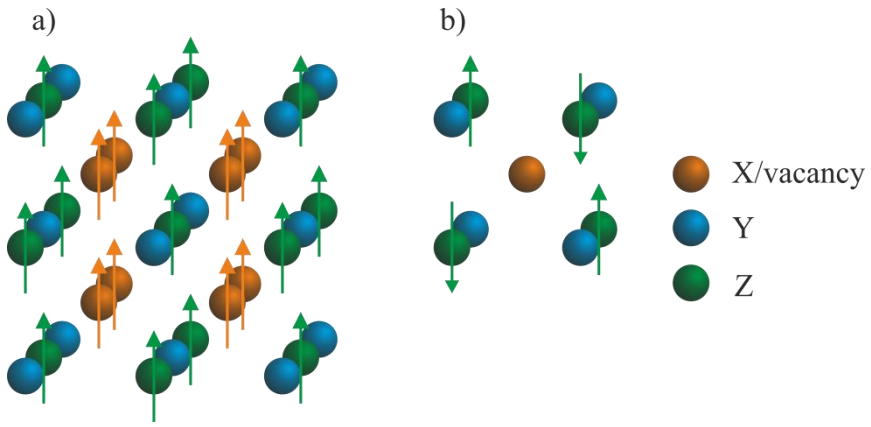

Figure 2.6: a) Ferromagnetic coupling of an $L2_1$ ordered X_2YZ Heusler alloy. b) Antiferromagnetic coupling of the YZ sublattice.

Antiferromagnetism has been experimentally measured in $L2_1$ and B2 structure full Heusler alloys as well as $C1_b$ structure half Heusler alloys [35]. The most common antiferromagnetic Heusler alloys have their magnetic moment due to Manganese at the Y site. In general the antiferromagnetic coupling is mostly favoured in B2-ordered structures because of the small Manganese nearest neighbour distances [40]. This leads to the challenge of fabricating partially ordered films which may require very specific growth conditions. Such growth conditions would then have to suitably order a ferromagnetic layer as well if exchange bias is to be successfully attempted using a sample consisting entirely of Heusler alloy magnetic layers. The $C1_b$ structure of half Heusler alloys leads to a large Manganese nearest neighbour distance. Therefore it is hypothesised that the coupling of the Manganese atoms is mediated by the electrons at the X or Z atomic sites [40]. Table 2.2 lists the antiferromagnetic Heusler alloys with Manganese at the Y-site.

X	Z	Crystal Structure
Cu	Sb	$C1_b$
Ni	Al	B2
Pd	Al	B2
Pd	In	$L2_1$-B2
Pd	Te	$C1_b$
Au	Zn, Cu	B2
Au	Al, Ga, In	$L2_1$
Pt	Al, Ga	$L2_1$
Ir	Al	$L2_1$
Ir	Ga	$C1_b$

Table 2.2: Antiferromagnetic Heusler alloys with Manganese at the Y site [35]

2.3 Antiferromagnetic ordering of selected compounds

2.3.1 The magnetic ordering of Ni_2MnAl

The study of Ni_2MnAl has attracted a great deal of attention as both ferromagnetic and antiferromagnetic ordering in both bulk and thin film samples has been reported [41, 42]. This mixture of ordering is considered to be a result of a mixture of $L2_1$ and B2 phases in the Ni_2MnAl lattice. Neutron diffraction by *Ziebeck and Webster* measured an antiferromagnetic cone spiral structure associated with the Manganese atoms along the (100) direction in a B2 ordered lattice [43]. Calorimetric measurements by *Gejima et al* on bulk $L2_1$ ordered samples provide evidence of ferromagnetic ordering [44]. *Acet et al* studied the effects of annealing on single crystals of Ni_2MnAl [45]. They found that annealing at T = 923K for 30 days created a stable antiferromagnetic B2 structure. Annealing at T = 653K for 30 days failed to produce a perfect $L2_1$ crystal as the compound has slow diffusion kinetics. *Acet et al* measured the Néel temperature of the B2 phase to be T_N = 313K and the Curie temperature for the $L2_1$ phase to be T_C = 375K. *Galanakis and Şaşioğlu* used *ab initio* electronic structure calculations to explain why the structure of Ni_2MnAl changes its magnetic ordering [41].

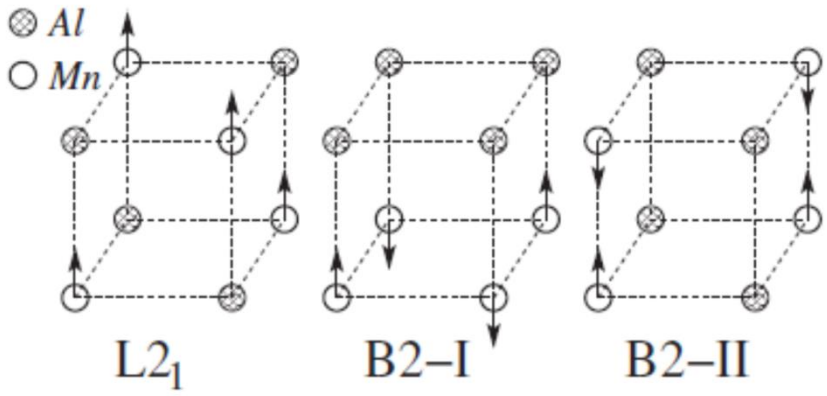

Figure 2.7: Structure dependent magnetic ordering of Ni_2MnAl [41].

Galanakis and Şaşioğlu considered two possible B2 configurations for Ni_2MnAl where the Manganese atoms lay in either the (100) or (110) plane. The arrows in figure 2.7 indicate the calculated orientation of the Manganese spin magnetic moments. The key difference between the $L2_1$ and B2 structures is the Manganese nearest neighbour distance. In the $L2_1$ structure Manganese atoms are separated by $a\sqrt{2}/2$ whereas in the B2 structure the Manganese atoms are separated by $a/2$ where a is the lattice constant. Therefore the Manganese atomic separation is 4.110Å in the $L2_1$ structure and 2.906Å in the B2 structure for an experimentally determined lattice constant of 5.812Å [45]. The smaller Manganese separation in the B2 structure then satisfies the conditions for antiferromagnetic coupling as predicted by the Bethe-Slater curve [12]. The Ni atoms in the B2 structure carry zero net spin due to the symmetry of being surrounded by an equal number of positive and negative Manganese spin magnetic moments.

The challenge in successfully using this Ni_2MnAl as a functional antiferromagnet lies in its growth process. This is because the magnetic properties are so sensitive to a relatively small change in the crystal structure. Therefore the growth process has to be optimal for the growth of B2 crystallites throughout the films produced. Ni_2MnAl is known to require high annealing temperatures in order to successfully crystallise the compound [45]. This may be unsuitable for devices as elements will diffuse across the interfaces. Interfacial coupling with a ferromagnet may also provide an interesting challenge because the orientation of the antiferromagnetic manganese atoms may not align with the interface. This means that a seed layer may be required to induce a preferred growth orientation in the film.

2.3.2 The magnetic ordering of Fe_2VAl

The study of Fe_2VAl has attracted the scientific community for both industrial applications and the understanding of fundamental physics [8]. This is because there have been several inconsistencies noted in the measurement of the electrical transport and magnetic properties of the compound [46]. *Nishino et al* [47] reported that the magnetic defects arise from variations in the Iron-Vanadium stoichiometry which were due to the heat treatment of the bulk samples used. This was supported by *Lue et al* [48] by measuring the specific heat of Fe_2VAl samples. *Popiel et al* [49] showed that the magnetic properties of Fe_2VAl depend on the crystal structure whereupon A2 structures are ferromagnetic but the B2 structure is superparamagnetic. *Venkatesh et al* [46] have supported this by performing *ab initio* calculations of $L2_1$ ordered Fe_2VAl whereupon several types of disorder were introduced to the unit cell. The calculations were then compared to magnetic measurements of DO_3-type Fe_2VAl which provided further evidence for the magnetic properties being dependent on the atomic disorder in the lattice sites.

Singh and Mazin [29] have predicted a stable antiferromagnetic state of Fe_2VAl when the compound is Iron doped to become $Fe_{2.5}V_{0.5}Al$. Their calculations were carried out using a supercell that was created by quadrupling the $L2_1$ structure along the (111) axis. This was done as the nearest neighbours of each atom were consistent with B2 ordering allowing for Iron and Vanadium atoms to be easily interchanged. The antiferromagnetic state was found by varying the composition of $Fe_{2+x}V_{1-x}Al$ and performing the calculations with antiferromagnetic ordering already in place. A metastable solution was found whereupon the Iron sites had an alternating moment of $\pm 2.3\mu_B$ or $\pm 0.6\mu_B$ whilst being antiferromagnetically coupled to each other. The work suggested that the Iron with the larger moment was acting as a quasi-free ion meaning that its spin arrangement was independent of the lower moment Iron atoms.

There has been some experimental evidence that the predicted antiferromagnetic state does exist. This was discussed by *Feng et al* [50] whereupon a lower than expected superparamagnetic response from a sample lead to the conclusion of antiferromagnetic states being present. Therefore if the growth conditions of $Fe_{2.5}V_{0.5}Al$ can be optimised to favour antiferromagnetic ordering in the thin films an exchange bias bilayer may be viable. At this stage it is unclear which type of crystal ordering will favour antiferromagnetic ordering. However based on the calculation parameters of *Singh and Mazin* B2 ordering may be preferential. It could be more likely for both ferromagnetic and antiferromagnet grains to co-exist in a polycrystalline sample as has already been demonstrated for Ni_2MnAl [45].

Chapter 3: Growth and Characterisation Techniques

3.1. Heusler alloy growth

The Heusler Alloys selected for this project had never been grown previously in York, as such a great deal of time was invested in optimising the growth conditions. Both 20nm and 100nm thick films were deposited on to Silicon substrates with a 5nm capping layer of either Tantalum or Ruthenium to be consistent with samples grown at Tohoku University as a part of the HARFIR collaboration. The substrates were cut by Agar Scientific prior to growth as 5mm x 5mm wafers for magnetic characterisation or 16mm x 16mm for structural characterisation in order to optimise the signal yield in the instruments available. Films were also sputtered on to Copper transmission electron microscopy (TEM) grids for analysis by T. Huminiuc. The grids were 3.05mm diameter square mesh purchased from Agar Scientific. The samples were annealed *ex situ* at temperatures ranging from 250ºC to 700ºC under 10^{-5}mbar vacuum in order to study their crystallisation.

The films were deposited using a Plasma Quest High Target Utilisation Sputtering system (HiTUS). Films were grown after pumping to a base pressure of less than 5×10^{-7} mbar. The Argon gas pressure to drive the plasma during sputtering was set at 1.86mTorr (2.5×10^{-3} mbar) using a mass flow controller. In order to prevent the system over heating, films were grown in 50 nm increments from an initial substrate temperature of less than 30ºC which typically rose to 80ºC during the process. X-ray reflectivity scans did not detect an interface as a result of this two-step growth process suggesting homogenous films are grown. The thickness and composition of the films were analysed via a range of techniques discussed later in this chapter whereupon the results were fed back in to the growth process in order to continually improve the quality of the samples.

3.1.1. The HiTUS system

HiTUS sputtering differs from conventional sputtering because in HiTUS the plasma is generated remotely from the target. This allows for around 95% of the target surface to be exposed to the plasma resulting in a high material flux and a greatly improved lifespan of the target typically of several years. Films are grown in this system at around 1Å/s due to the relatively large (300mm) distance between the target and substrate. This is because the material sputters in a conical profile leading to a high growth rate dependence based on the proximity of the sample to the target. The high growth rate produces uniform films with less than 2nm peak to peak roughness. Another advantage of the large separation is that the substrate is kept out of the plasma beam. As a result there is no re-sputtering from the substrate during deposition removing any complicated substrate growth parameters such as Silicon embedding in to the Heusler alloy structure. The films grown are polycrystalline which allows for comparison with the properties of films grown in the data storage industry.

The HiTUS system has a number of advantages that allow for a wide range of film structures to be achieved. Alloys are well suited to being sputtered in the HiTUS as the entire target surface is eroded allowing a comparable stoichiometry between a powder metallurgy target and the thin film. Up to 8 different elements or alloys can be loaded in the target carousel without breaking vacuum allowing for complex multilayer structures to be created. The substrate carousel can be loaded with up to 6 samples which can hold four 5mm x 5mm substrates or a single 20mm x 20mm substrate, both with TEM grids. It is also possible to load other geometries or circular substrates in the system. The HiTUS uses rotary, turbo and cryo-pumps to reach $5x10^{-7}$mbar pressure in around two hours which, when considered with the sputter rate, allows for up to three full growth sessions to be completed per 24-hour cycle.

The HiTUS generates the plasma in a side arm consisting of a 2.5kW, 3-turn copper radio frequency (RF) antenna in a quartz tube that is surrounded by a Faraday cage (figure 3.1). The Argon gas is inductively coupled to the 13.56MHz RF field generating a plasma. The plasma is then launched into the main chamber by the launch electromagnet. As the ions follow the launch flux in to the chamber the field from the steering magnet directs the flux, and hence the plasma ions, towards the target surface. This process is known as ambipolar diffusion [51]. The resulting plasma has a high ion density of 10^{12}-10^{13} ions/cm^3 however the low ion energy (<10eV) at the target surface is insufficient for sputtering [52]. In order to increase the ion energy to enable sputtering, the plasma is coupled to a DC bias voltage.

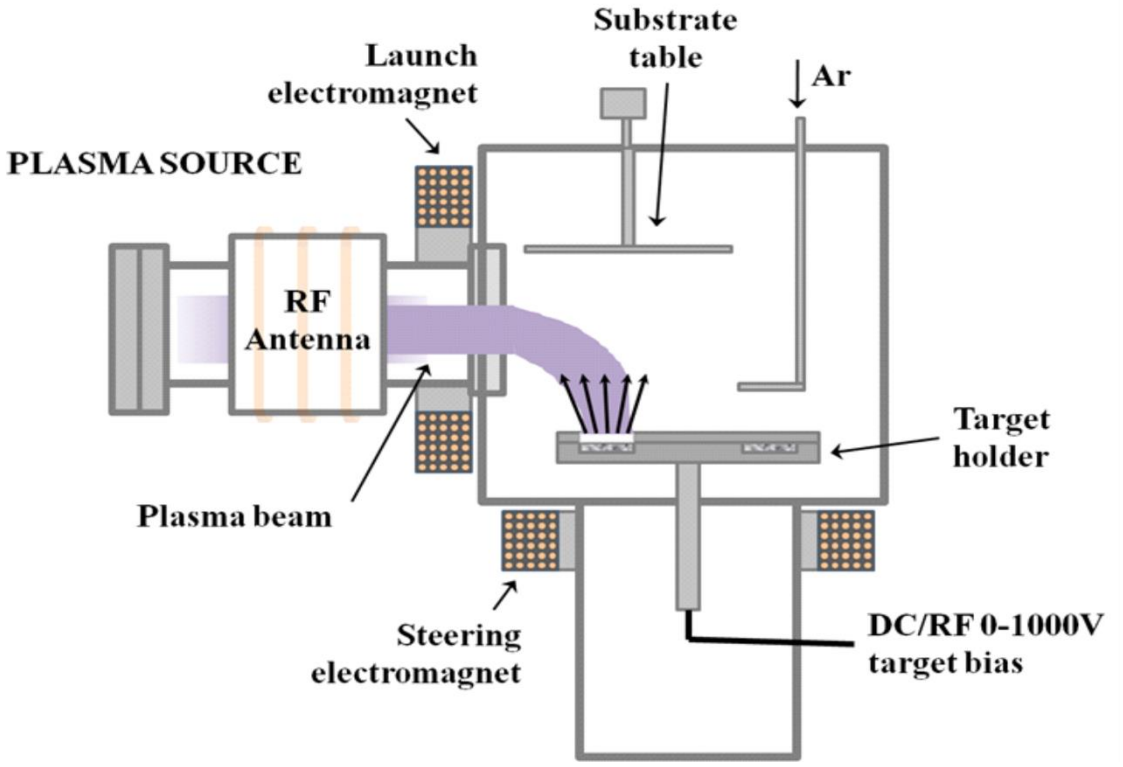

Figure 3.1: A schematic of the HiTUS

In order to compare the properties of thin films a number of sputtering parameters have to be controlled. The plasma pressure can be controlled by varying the Argon gas flow into the system which affects the sputter rate because there is a change in the mean free path of ions and film density due to Argon contamination and deposition energy. The energy of the ions can be initially controlled by setting the launch RF power at 1 to 100% of a 2.25kW capacity. Within the chamber the ion energy can be controlled at the target surface by the applied DC bias voltage. Each of these parameters can also change the mean grain diameter of the film which is important for interpreting magnetic measurements [53]. It should be noted that disabling the steering magnet floods the main chamber with ions of energy <30eV which are useful for cleaning surface contaminants from the substrates prior to film deposition [53].

York is currently the only institution growing Heusler alloys via the HiTUS process resulting in several recent publications [30, 51, 52]. Heusler alloy thin films grown in the HiTUS system are unique as unlike magnetron and MBE films, the samples exhibit little or no crystallisation in the as-deposited state. Previous work by *Sagar* and *Fleet* [32, 54] has shown that annealing the films *ex situ* allows large crystals, or grains, to grow from the as-deposited amorphous matrix. After annealing Co_2FeSi films for up to 6 hours the median grain diameters were measured to be between 30nm and 250nm [32]. Fleet *et al* [32] suggests that this process is

a result of layer by layer crystallisation seeded by nano-crystal nucleation in the as-deposited matrix. The Heusler alloys used in this project required much more extreme annealing conditions to successfully crystallise with temperatures typically exceeding 600°C in thirty minute intervals to monitor Silicon segregation from the substrate. In previous work, crystals in the films have shown a large variation in crystallographic orientation [55] however as discussed in the result chapter, the films in this project exhibited columnar growth perpendicular to the substrate.

3.1.2. Calibrating the film thickness

The HiTUS system uses an INFICON XTM/2 deposition monitor to measure the thickness of the film during deposition. The device works by oscillating a piezoelectric quartz crystal at its electromechanical resonance. Depositing small amounts of material onto one face of the crystal causes the resonant frequency to be reduced via the following relationship:

$$M_f / M_q = (\Delta F) / F_q \tag{3.1}$$

where M_f is the change in mass due to the deposition, M_q is the original mass of the quartz crystal, ΔF is the change in resonance frequency and F_q is the uncoated resonant frequency of the crystal [56]. The INFICON XTM/2 deposition monitor calculates the thickness of the deposited layer t_{film} by the Z-match equation:

$$t_{film} = \left(N_{at}\rho_q / \pi\rho_f F_c Z\right) arctan\left(Ztan\left[\pi\left(F_q - F_c\right) / F_q\right]\right) \tag{3.2}$$

where N_{at} is the frequency constant of the quartz, ρ_q is the density of the quartz, ρ_f is the density of the deposited film, F_c is the quoted resonant frequency of the quartz and Z is the acoustic impedance ratio [57]. For each material being sputtered the density and the Z-ratio must be entered to allow accurate an calculation of the layer thickness.

The technique to measure the film thickness was first used by *Aley* [58] whereupon the deposited mass of the film was measured using a Mettler-Toledo microbalance with a 0.01µg accuracy. Glass substrates of 10.0mm diameter and 0.2mm thickness were chosen because the large surface to edge ratio minimised any error in the thickness calculation by deposition on the side of the substrate. The substrates were cleaned and measured before and after deposition with the resulting difference in mass was used to calculate the thickness of the layer. The density of the thin films was calculated from the accepted bulk values of the individual elements in the compound. Films were sputtered at thicknesses of 20nm to 100nm as measured on the quartz crystal monitor in the HiTUS. The resulting plot comparing the measured film thickness and

expected film thickness provides a comparative indication of the quantity by which a film is under or over sputtered.

X-ray reflectivity and energy dispersive X-ray spectroscopy (EDS) data were also used to measure the thickness of the thin films in an effort to test the accuracy of each technique. The principle aims of these measurements and their operating principles are discussed later in this chapter. Both of these techniques are based on physical models and operate by fitting the calculated response of an idealised sample structure to the measured experimental data via a least squares fitting process. Although these techniques are not true direct measurements it is useful to check their validity in the event of any unexpected results that arise. For example anomalous results were obtained using EDS however the thickness measurement remained accurate when compared to results from other measurement techniques.

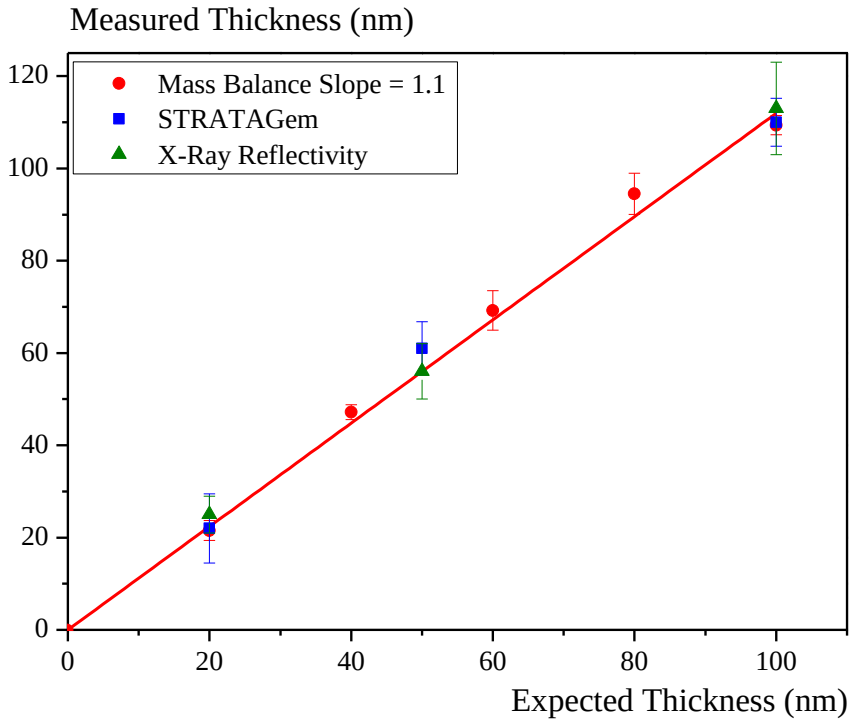

Figure 3.2. The deposited thickness of Fe_2VAl

It can be seen from figure 3.2 that all of the measurement techniques agree within error. The expected thickness refers to the thickness as measured by the quartz crystal monitor in the HiTUS. This result was unexpected as *Aley* [58] suggested in his thesis that the excess thickness was due to the films being around 90% as dense as the bulk values used to calculate the measured thickness. If this was true, the reflectivity and EDS data would fit on a different slope if the density used in the thickness calculation was incorrect because both techniques calculate the film thickness independently of assumptions from bulk densities. Therefore the most likely explanation for the expected thickness to be inaccurate is that the tooling factor (*TF(%)*) was not

correctly set. The tooling factor is a correction of the sputtering rate which is due to the quartz crystal and the sample substrates being held at different angles and distances to the target.

The technique for calculating the tooling factor was first used by *Aley* [58] whereupon he deposited half covered substrates to produce thin films with a step profile. A profilometer was then used to measure the step heights which led to the tooling factor being calculated by:

$$TF(\%) = TF_{initial}\left({}^{t_{actual}}/_{t_{crystal}}\right) \tag{3.3}$$

where t_{actual} is the actual thickness deposited on the substrate, $t_{crystal}$ is the thickness recorded by the crystal rate monitor and $TF_{initial}$ is the tooling factor that was input to the crystal monitor at a value of 100. During this work a profilometer was not available which lead to the three techniques discussed in this section being used. The gradient of the resulting plot shown in figure 3.2 was the method used to measure ($t_{actual}/t_{crystal}$). The densities in table 3.1 were calculated from the bulk densities of the individual elements within the alloy.

Heusler Alloy	Density (g/cm^{-3})	Deposited Thickness	Tooling Factor
Fe_2VAl	6.095	10% extra	110
Ni_2MnAl	6.951	20% extra	120

Table 3.1: The thickness calibration for the HiTUS system.

3.2 X-ray crystallography

3.2.1 Crystal structure

X-ray diffraction is a powerful tool for analysing the structure of crystalline materials and was developed by Von Laue in the early 20th century for which he was awarded the Nobel Prize in 1914 [59]. A Rigaku SmartLab X-ray diffractometer was used to characterise the crystal structure of the thin films [60]. The SmartLab houses a 9kW rotating Copper anode X-ray generator that produces a 0.4 x 8 mm X-ray beam. In order to maximise the measurement signal the films were sputtered on to 16 x 16 mm substrates in order to utilise the full profile of the X-ray beam. All measurements were carried out using a parallel X-ray beam configuration. The X-ray source and detector were mounted on a 5-axis goniometer allowing for several different scanning geometries. There are also multiple sample stages available for tilting or translating the sample. As there are several possible configurations available the optical components for each type of measurement used in this project are detailed in table 3.2 with reference to figure 3.3.

Soller slits and a PSA adapter were used to columnate the X-ray beam for the measurement of polycrystalline thin films and also to set the resolution of the measurement as listed in table 3.2. The incident parallel soller (IPS) adapter and monochromator were used to set the resolution of the incident beam. The monochromator used a Germanium (220) crystal to achieve high resolution however this resulted a significant loss of signal which made the component impractical for measuring the samples.

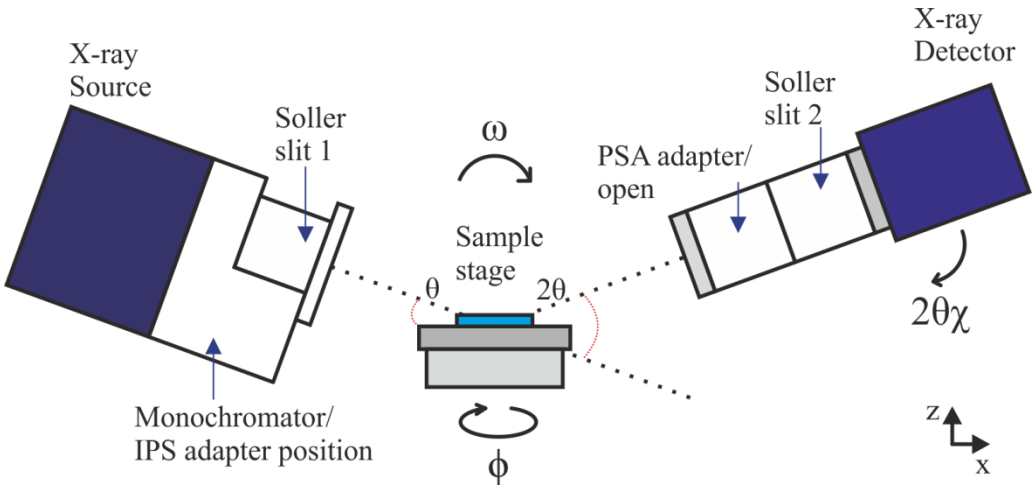

Figure 3.3: A schematic of the SmartLab X-ray diffractometer. The ϕ (sample rotation) and 2θχ (2θ detector arm in *xy* plane) axis rotate about the z-axis of the tool and the ω-axis rotates about the y axis of the tool.

The samples were aligned for crystal structure measurements using the direct-beam half-cut alignment technique. This works by scanning the sample along the z-axis in order to ensure the sample height was placed half way in to the X-ray beam. After z-alignment the sample was aligned over the ω axis so that the critical angle of the reflectivity scan had the maximum X-ray counts available. At this point the samples were considered to be parallel to the X-ray beam. In order for measurements to be comparable it was important to ensure that the same integration time was set during scans in order to allow peak intensities to be directly compared against each other. The integration times were determined by combining the scan speed and step size settings that were input in to the SmartLab. For each measurement technique the settings were chosen based on maximising the signal yield within a reasonable timescale of around 90minutes per θ-2θ scan. Table 3.2 lists the integration times used for the scans.

In order to characterise the crystal structure of the samples two parameters were investigated: the lattice constant and the Q factor. Each sample was first measured with a theta-2 theta (θ-2θ) scan to check for the degree of crystallisation. Any observed peaks were then fitted using a lognormal function. This was because the scans had an asymmetric background profile

that could be fitted effectively using lognormal fitting parameters. It should be noted they pseudo-Voigt and Gaussian profiles were also tested however lognormal fitting provided the most repeatable data. The peaks were characterised using Bragg's law to obtain the interplanar spacing [61] of characteristic peaks. The lattice parameter of the Heusler alloy films was then calculated from the measured (220) interplanar spacing. The (220) reflection was chosen as is the main reflection for the Heusler alloys studied which provided the greatest number of counts per unit of scan time. This minimised the error in the determination of peak position and width. The Q factor was used as a method to compare the crystal quality between films within the HARFIR group. A high peak intensity was considered to be indicative of a large number of crystallites and a lower FWHM was indicative the degree of epitaxy of the film. Therefore a high Q factor described epitaxial samples like those that could be produced by MBE by the HARFIR partners in Tohoku. However the films produced in this project had a low Q (<1500) which indicated that they were polycrystalline and did not have a large number of well-ordered grains. The grain sizes of the films had to be determined by TEM because it was the standard practice for all students in the group. The TEM measurements were to be conducted by other HARFIR students and are not included in this work.

$$n\lambda = 2d \sin \theta_D \tag{3.4}$$

$$Q\ factor = {}^{Peak\ intensity}/_{Peak\ FWHM} \tag{3.5}$$

where n is the order of diffraction, d is the planar spacing, λ is the X-ray wavelength and θ_D is the angle of diffraction. By using simple trigonometry and the measured lattice spacing it is possible to obtain the lattice constant. The peak top positions were obtained by finding the minima of the second derivative of the fitted peak. Repeatedly fitting a well-defined (Q > 1000) Ni_2MnAl (220) peak using this technique gave a reproducibility of 0.01Å for the measured lattice constant.

Once the lattice constants for the different layers were determined, the (220) peak of the Heusler alloy was scanned using a rocking curve. To do this, θ-2θ was locked at the (220) peak position measured in the initial θ-2θ scan and then the sample was scanned over the ω-axis. By scanning over the ω-axis the (220) peak can be detected for grains that are not aligned perpendicular to the substrate. The full width half maximum (FWHM) of a rocking curve peak provides a measurement of the distribution of crystal orientations. Further texture mapping is possible with the SmartLab by measuring a reciprocal space map to obtain 2-dimensional information about the thin film structure but highly ordered samples are required.

Scan Type	Soller Slit (º)	Step Size (º)	Speed (º/min)	PSA (º)
θ2θ	5.0	0.05	0.35	5.0
Rocking Curve	5.0	0.10	3.00	None
Reflectivity	5.0	0.05	5.00	None
Pole Figure	0.5	3.00	150.00	In-plane 5.0

Table 3.2: The optics and scan settings used for X-ray measurements in this project.

3.2.2. Crystal orientation

Polycrystalline materials are composed of crystalline grains which in general are randomly orientated. However the materials produced in this work are known to have texture. For example cross-sectional transmission electron microscope images by *Chureemart* [62] and *Sagar* [54] have demonstrated that some samples have a preferred orientation. If a sample does have a preferred orientation then a conventional θ-2θ scan may not describe the crystal texture accurately because the scan only measures the grains that are normal to the sample surface. Therefore the presence of a preferred orientation requires further mapping which can be determined by a pole figure scan [63, 64]. In order to perform a pole figure scan a known diffraction line must be selected such as the (220) Heusler alloy peak. The sample is then rotated in all directions as demonstrated in figure 3.4 to construct a hemispherical map of the diffraction space. A detailed description of the sample alignment procedure can be found in section 3.2.3. The α and β angles correspond to the ω and ϕ angles in figure 3.3 respectively.

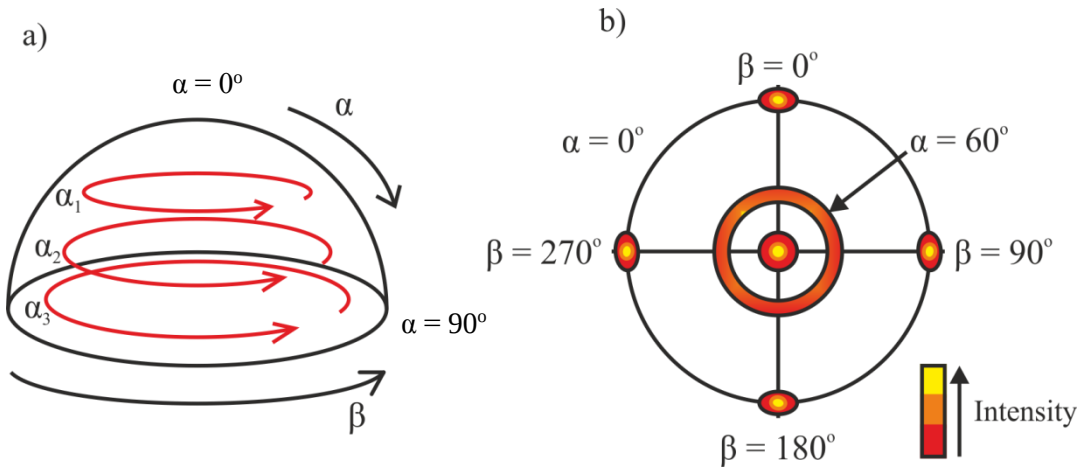

Figure 3.4: a) Schematic of the pole figure scan geometry b) A projection of a pole figure scan measured in the (2 2 0) plane for a *fcc* crystal on a (1 0 0) single *bcc* crystal substrate.

A pole figure scan reveals a number of characteristics of a sample. In order to understand some of the data in section 4, knowledge of the measurement procedure is required. Firstly the θ-2θ scan was set at the (220) diffraction angle for the pole figure scan and as expected a peak was measured at $\alpha = 0^{o}$ corresponding to the peak measured from a θ-2θ scan. There is a ring at $\alpha = 60^{o}$ arising from the equivalent (202) plane in the symmetric *fcc* structure of the film. The presence of the ring denotes fibrous texture. Therefore the figure suggests that the sample (220) plane is normal to the sample surface. The spots on the $\alpha = 90^{o}$ contour are likely to be from the single crystal substrate because the diffraction space that has been scanned encompasses the substrate (100) plane according to the crystal simulation discussed in section 2.2. Discussion of pole figure scans later in the results chapter will be in the context of other X-ray scans.

3.2.3. X-ray reflectivity

X-ray reflectivity is a surface-sensitive measurement technique that can be used to characterise the thickness, density and roughness of thin film layers [64]. The technique was first used by Parrat to measure the depth of oxidation in evaporated Copper films [65]. In reflectivity and pole figure scans the samples are aligned by performing a grazing incidence scan to find the 2θ angle of total reflection from the sample. A rocking curve was then measured over this point to observe specular reflection. This was because the peak position of the specular reflection curve indicates the half-way point of the total reflection angle which increases the accuracy of the 2θ setting [63]. At that point ω was aligned to the rocking curve peak top and the sample tilt was varied using a mechanised sample stage. This process was repeated until the maximum signal output for ω was achieved which indicated the plane of the sample surface was aligned to the plane of the incident beam. The X-ray beam struck the sample at a low grazing angle of and the intensity of the reflected X-rays was measured as the incident angle was varied whilst being fixed relative to ω. This resulted in a $2\theta/\omega$ scan in the range of $2\theta/\omega = 0^{o}$-5^{o}.

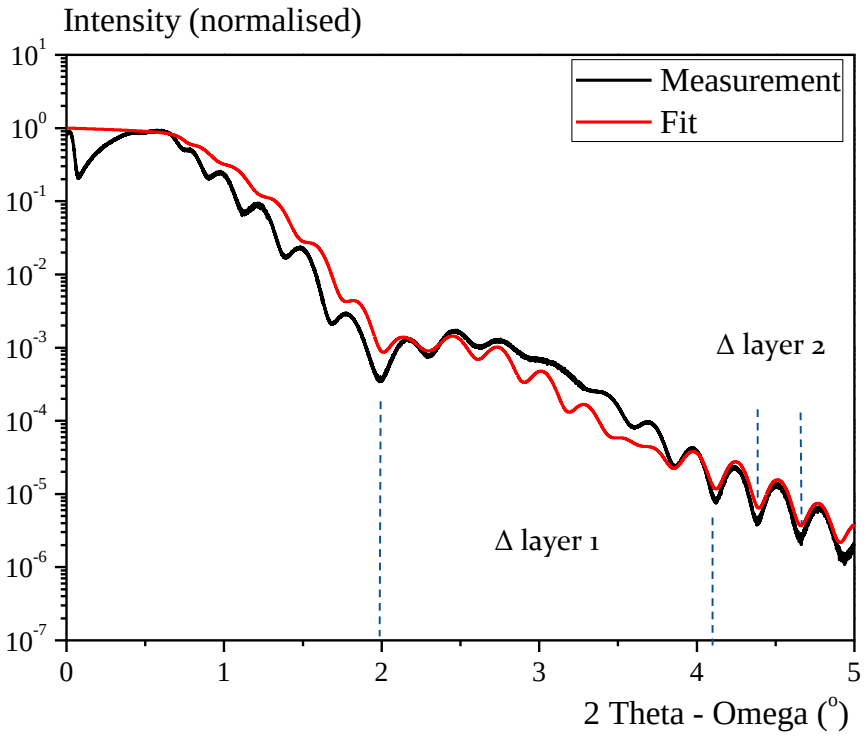

Figure 3.5: Fe_2VAl reflectivity profile fitted by the Rigaku GlobalFit Software package [66].

Figure 3.5 is a typical X-ray reflectivity measurement that has been fitted using the Rigaku Global Fit software package which calculates the density, thickness and roughness of layers in a sample. The profile of the scan region below the critical angle is characteristic of the sample shape and its alignment within the diffractometer which cannot be modelled. The software operates by least squares fitting a simulated profile to the experimental data. As a result of this a great deal of intuition and time was required to achieve a well fitted profile. For example a 2nm SiO_2 was added to the schematic of the sample and the roughness of the films was estimated from cross-section transmission electron microscopy images of Heusler alloys by *Sagar* [54]. The equations used in the fitting had not been released by Rigaku as they are kept as intellectual property and therefore cannot be stated. The software was unable to provide a high quality fit of the reflectivity curves. The fit was optimised adding an oxide layer above the substrate because the period of the fringes to have two modulations which indicates that the profiles of two layers are interfering [67]. A schematic of these modular components is labelled as layer 1 and layer 2 on the graph. The density of each layer was fixed at a value calculated from the bulk instead of being calculated by the software in order to increase the repeatability of the results. The roughness and thickness parameters of the sample were then varied manually and the fitted values were taken for a minimum of 10 trials. The values obtained for the Fe_2VAl layer thickness agreed within error with the direct measurement as described in section 3.1.2.

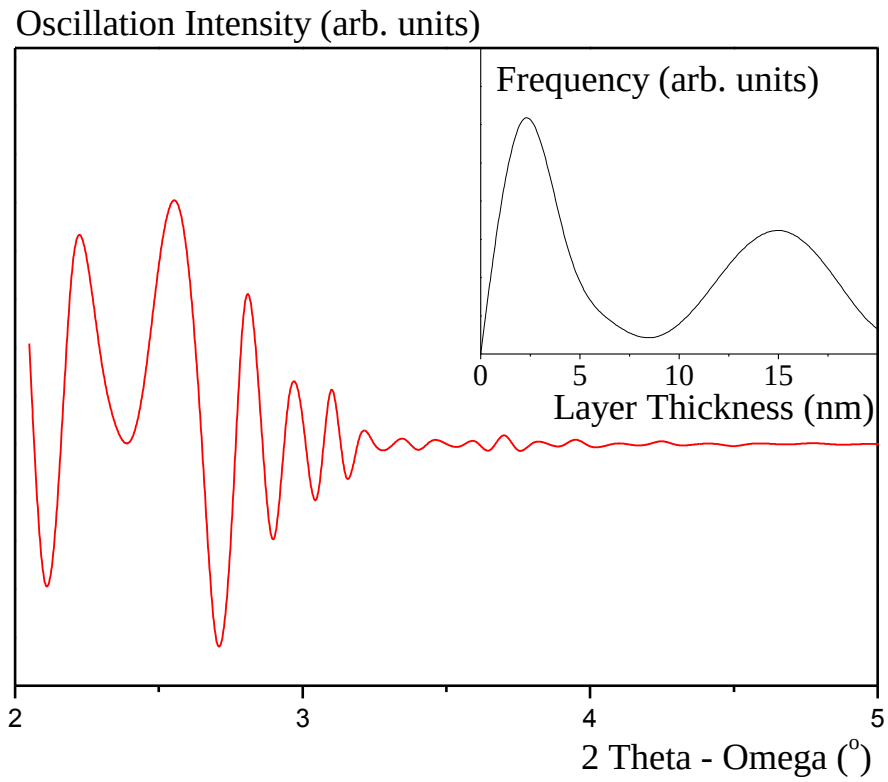

Figure 3.6: Extracted oscillation curve of Figure 3.5 with a Fourier transform of the oscillation curve inset in the top right of the figure.

A fast Fourier transform was carried out in an attempt to directly measure the thickness of the Fe_2VAl layer using a technique published by Rigaku [67]. The calculation was carried out at 2 Theta – Omega greater than 2° in order to minimise the effect of fringes shifting near the critical angle as a result of diffuse scatter [64]. Figure 3.6 shows the result of the Fourier transform-based technique when used on the data shown in Figure 3.5. It is clear from the Fourier transform that two periods exist which are identifiable in the figure by different oscillation periods from 2.0°-2.7° and 2.7° onwards. The two layer peaks were fitted multiple times using a Gaussian peak model resulting in thicknesses of (3.0 ± 0.2) nm and (14.9 ± 0.2) nm being obtained. This supported the idea discussed previously that an oxide layer did exist within the sample however the thickness of the Fe_2VAl layer was less than expected when compared with the other thickness measurement techniques used. This could be due to the relatively weak fringe contrast from the Fe_2VAl 2.0° to 4.0° caused perhaps by roughness at the interface or a dominant signal from the oxide layer. Therefore scanning at a higher angle would be useful for improving this technique if there is sufficient signal. This technique could be used to support the GlobalFit software package in obtaining the density and roughness of the layers from conventional XRR fitting as was recommended in the details of the published technique.

3.3 Magnetic measurements

The crystalline order of Heusler alloys can dramatically affect their observed magnetic properties. For example, the $L2_1$ phase of Ni_2MnAl is ferromagnetic whereas the B2 phase is antiferromagnetic [45]. Therefore once the crystal growth of the Heusler alloys was optimised the magnetic properties were then measured. The ferromagnetic and bilayer F/AF samples were characterised magnetically by measuring the magnetic response of the samples in the form of an M-H hysteresis curve. In theory successful exchange coupling between the ferromagnetic and antiferromagnetic layers is observable via a change in H_c or a hysteresis loop shift H_{ex} when field cooled. Therefore bilayer samples were measured at room temperature and at liquid Nitrogen (77K) temperatures as an initial test to see if any exchange coupling was present. Characterisation of antiferromagnetic thin films is difficult however a detailed experimental procedure has been developed to obtain repeatable and accurate results of exchange bias [68, 23].

3.3.1. The vibrating sample magnetometer

The vibrating sample magnetometer (VSM) is the most commonly used instrument for measuring the magnetic properties of thin films and nanoparticles. The VSM was invented by *Foner* in 1955 [69] after improving on Smith's vibrating coil magnetometer [70, 71]. Typically VSM's have an operating range of ± 20 kOe with some modern systems being able to exceed ±100 kOe with a typical noise floor of 10^{-7}emu and a large sample temperature range of <4.2K – 1000K which is achievable because the simple arrangement of the equipment allows for easy installation of a cryostat and oven [72]. Systems are commonly equipped with automated temperature and sample angle control [73] resulting in an unparalleled versatility for magnetometry applications. Some VSMs are available with multiple detection coils configured for vector analysis of a thin film sample and allowing magnetoresistance measurements [72].

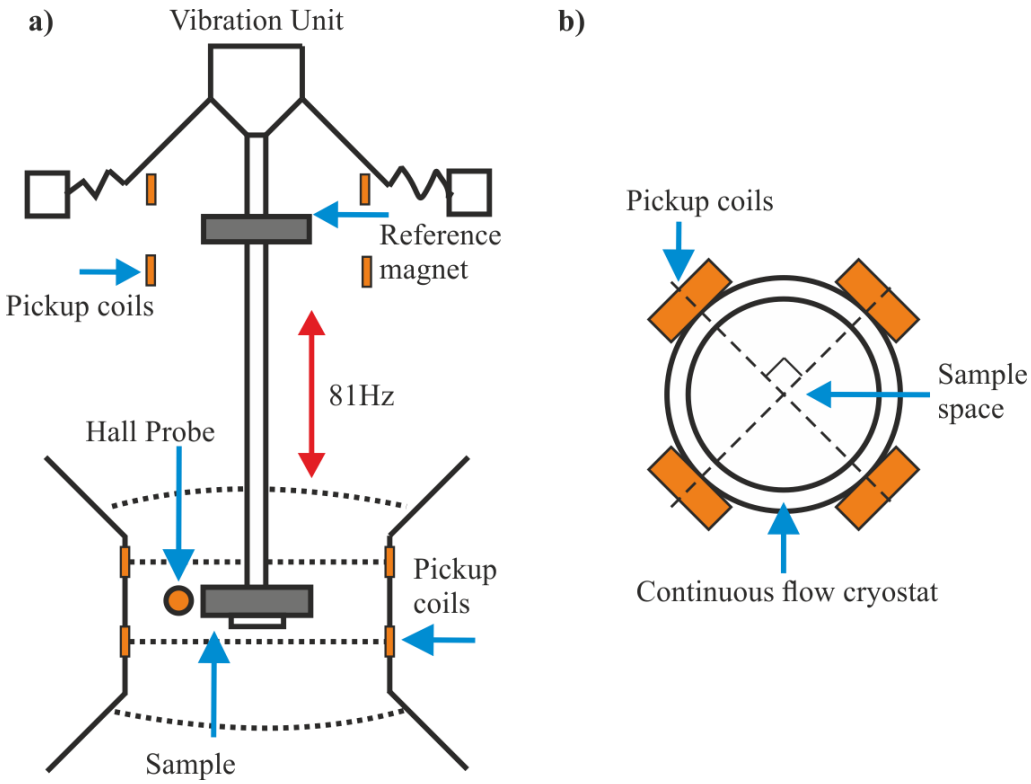

Figure. 3.7. a) A schematic of a typical VSM. **b)** A plan view schematic of the pickup coil configuration in the York VSM.

A Micro Sense Model 10 VSM [73] was used in this project as shown in figure 3.7. It operates by placing a sample in an applied magnetic field and oscillating it at 81Hz which can be measured using pick up coils. The frequency of 81Hz is used because there are no harmonics in the laboratory that could cause noise in this measurement range. A permanent magnet is used as a phase reference which is mounted at the top of the non-magnetic oscillating column and measured through a matching set of pick up coils. As the phase of the sample is matched to the reference magnet the AC signal generated can be measured easily by using a digital signal processing (DSP) lock-in amplifier. The system is calibrated using a Palladium film with similar physical dimensions to the sample and a known moment of 3.88 x 10^{-7} emu/Oe/f.w (formula weight). [10]. This is an effective calibration technique because Palladium is a Pauli paramagnet whose magnetisation is linearly proportional to the applied field and whose susceptibility is largely independent of temperature. This proportionality is due to the sample moment being due to the conduction electrons in the Palladium aligning with the applied field. The response of the sample is compared to this calibration which leads to an accurate comparator measurement described by equation 3.6:

$$V_{emf} = -N \, {}^{d\emptyset_M}/_{dt} \propto m \qquad (3.6)$$

where V_{emf} is the induced electromotive force, N is the number is turns in the pickup coil, $d\emptyset/dt$ is the rate of change of flux and m is the magnetic moment of the sample. This relationship can be explained physically as the VSM pickup coils are mechanically coupled to the reference magnet and sample. This means that the change in flux registers as a voltage change in the system due to the *emf* produced. The magnitude of the change in flux is proportional to the magnetic moment of the sample. The magnitude of this proportionality has been calculated by calibrating the VSM using Palladium. Hence the moment of the sample can be calculated from the measured voltage. This process is repeated at different values of the applied field in order to plot M-H curves for a given sample. The minimum field resolution of this instrument is 0.01Oe in the range of ±300Oe. The temperature of the sample is stable to ±1K over 60 minutes.

In order to minimise error, the detection coils are arranged in pairs and counter wound so that their resulting signal is effectively zero when there is no detectable signal. The coils are connected in series to reduce the error in measuring the positioning of the sample. The Model 10 VSM uses four pairs of coils mounted on opposite sides of the sample. These coils are mounted orthogonally as the arrangement has been shown to be insensitive to signals that may arise from stay fields and to account for any non-uniformity in the applied field [74]. The applied field is measured by a Hall probe that has been calibrated against a Bell Series 9900 Gauss meter which is a secondary standard. It is important to stabilise the oscillation of the sample to ensure there is no imbalance in the change of flux from one coil pair to the other. Therefore the VSM is isolated from outside vibrations and the sample rod is stiffened to ensure there is no sample movement in the *x-y* plane.

3.3.2 The alternating gradient force magnetometer

The alternating gradient force magnetometer shown in figure 3.8 (AGFM) is a highly sensitive magnetometer that is ideal for measuring large numbers of samples. The AGFM was first proposed by *Zijlstra* in 1970 [75] however Princeton Measurements Corporation who are now a part of Lakeshore Inc. were the first to manufacture commercial AGFMs in the 1980's [76]. They are popular instruments because their relatively simple design boasts a high sensitivity of 10^{-8}emu with a high field sweep rate allowing hysteresis loops to be measured in field ranges of ±20kOe in 90 seconds. The standard measurement package available has a wide range of applications for the measurement of multi-layer magnetic thin films and ferrofluids [77] in the applied field plane direction.

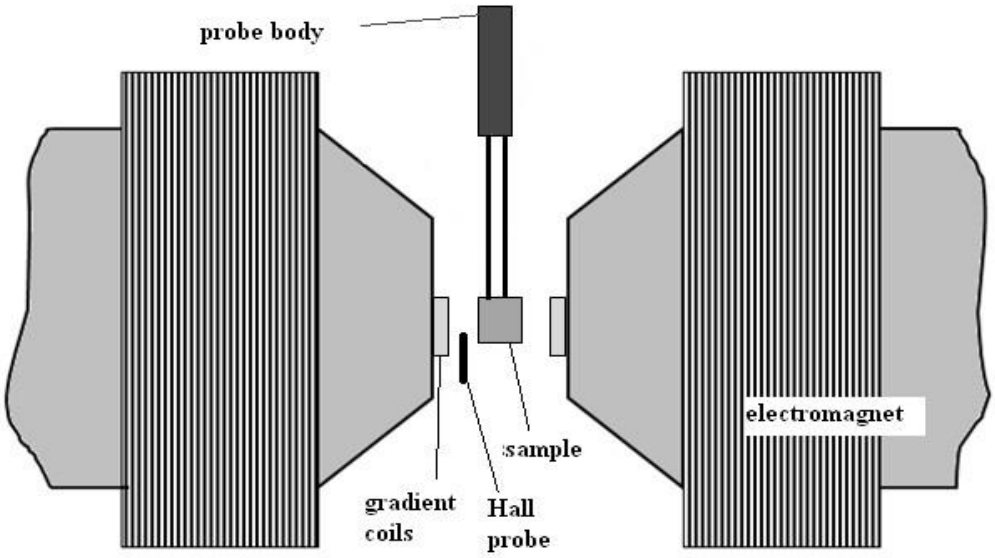

Figure. 3.8: Schematic of the AGFM

The AGFM operates by measuring the force exerted on a sample that has been placed in an alternating field with a gradient produced by two north to north driving coils [75]. Initially the force was measured using an optical microscope to view the displacement of the sample however Reeves introduced a piezoelectric detector to measure the force directly in 1972 [78]. The design of the AGFM is a extension of the design of *Roos et al* using a piezoelectric bimorph to measure the sample resulting in a system with a noise base of 10^{-11}emu [79]. The system operates by mounting the sample on two thin quartz tubes of equal length which are glued to a piezoelectric bimorph. Any offset in the sample position produces a measurable voltage by straining the bimorph. The low noise base is achievable because the alternating field is applied at the resonant frequency of the quartz tubes which gives the system a Q-factor typically over 30. The signal is processed using a DSP lock-in amplifier whereupon the resulting system response is described by [80]:

$$F_M = -V_S M.\nabla B_0 = -m\sigma.\nabla B_0 \tag{3.7}$$

In this equation V_S represents the sample volume, m represents the sample mass, M represents the sample magnetisation, F_M represents the force on the sample and σ is the standard deviation of the log normal distribution of the mean sample grain volume. The field gradient, represented by ∇B_0, *i*s controlled by varying the current through the gradient coils that are placed at the magnet pole caps. The system is calibrated with a Palladium foil of similar dimensions to the sample.

There is a limitation to using the AGFM that arises from using a field gradient to measure a magnetic sample. The gradient coils are set north to north with a standard operational field gradient of 4 Oe/mm which for a typical 5mm x 5mm thin film results in an AC field at the sample edge of 10 Oe. This value is not insignificant as samples with a low coercivity can be demagnetised non-uniformly. To reduce this effect, lower field gradients of 0.4 Oe/mm and 0.04 Oe/mm can be used. However use of these lower field gradients reduces the signal of the measurement due to there being less force across the sample. The AGFM is also highly sensitive to acoustic vibration whereupon general laboratory noise can be seen in a measured hysteresis loop. As a result of this sensitivity it is impossible to conduct temperature controlled measurements in the AGFM as the vibrations from a medium such as liquid nitrogen will overload the signal arising from any magnetic response in the sample.

3.4 Measuring the thin film composition

Controlling the composition of the Heusler alloy thin films is critical for achieving the desired antiferromagnetic ordering required to produce exchange biased devices. For example *Singh* and *Mazin* predicted that Fe_2VAl is a ferromagnetic compound whereas $Fe_{2.5}V_{0.5}Al$ forms a metastable antiferromagnetic state [29]. The targets used in the HiTUS were ordered to the specification of a full Heusler alloy X_2YZ stoichiometry however due to different sputtering rates of the individual elements in the powder metallurgy targets the composition has to be carefully monitored. A Thermo-Scientific UltraDry EDS detector mounted on a FEI Sirion scanning electron microscope (SEM) was used to measure the sample composition. An optimised measurement procedure was developed and then the data from the instruments was analysed using a specialised software package named STRATAGem [81]. The procedure was checked for accuracy by sending reference samples to a company named InterTek [11] for ISO9001 standard chemical analysis.

3.4.1. X-ray microanalysis and scanning electron microscopy

The scanning electron microscope (SEM) is a widely used instrument that is very versatile for analysing nanoscale structures. It was pioneered by *von Ardenne* in the early 20th century [82, 83, 84] who took the first high magnification (10nm area) images of samples. Modern SEM's can typically achieve 1nm resolution and house a multi-sample stage that can be rotated and tilted for 3-dimensional characterisation of samples [85, 86]. Typically several detectors are housed within the SEM chamber in order to obtain different characteristics about a sample's morphology and chemical structure. Samples can be probed with an electron beam accelerated at a large range of energies from less than 0.1keV to more than 30keV. When the electron beam is accelerated in

this energy range the electrons have sufficient energy to generate characteristic X-rays to be emitted by the sample, thus allowing the composition of the sample to be studied. This is known as energy dispersive X-ray spectroscopy (EDS).

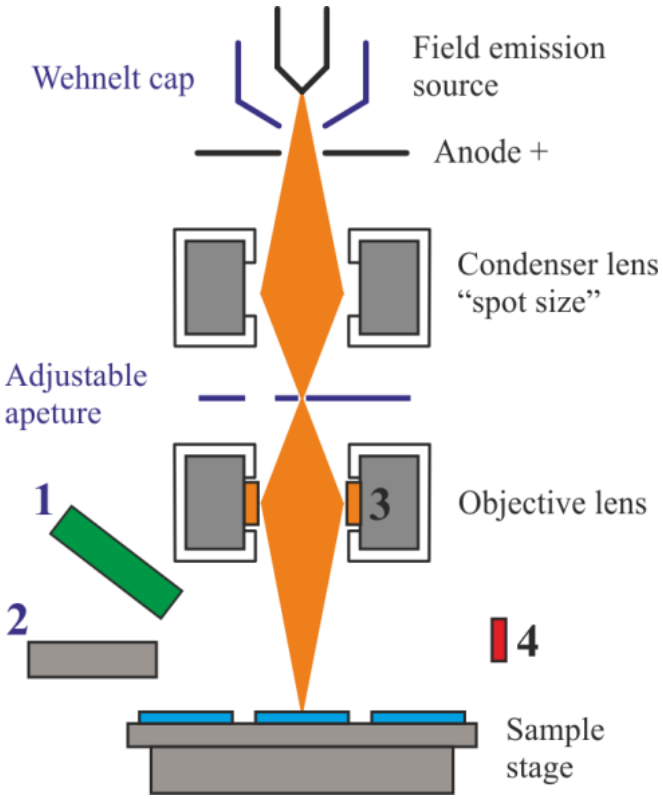

Figure 3.9: A schematic of the Sirion S-FEG SEM chamber, the detectors are labelled as 1) energy dispersive X-ray detector 2) secondary electron detector 3) in-column ultra-high resolution secondary electron detector and 4) a CCD camera.

A Sirion S-FEG field emission SEM was used in this project as shown in figure 3.9. It operates by generating electrons from a tungsten filament via the process of field emission. The electrons are then focused by a negatively biased (-200V) Wehnelt cap to create a beam that appears to be emitted from a circular emission region. The beam is then accelerated through a highly biased (1-30kV) anode. The condenser lens controls the beam divergence or "spot size" prior to the mechanical aperture. A larger spot size setting increases the beam current by focusing more electrons through the mechanical aperture. The objective lens is then used to control the area of the electron beam illuminating the sample surface. For EDS the samples were measured at 200x magnification which was equal to an area of 1800μm^2 in order to maximise the yield of X-rays. At the start of each measurement the objective lens was finely tuned along with the sample stage position in order to ensure that the sample was in the focal plane of the electron beam.

A Thermo Scientific UltraDry energy dispersive spectrometer was used to measure the characteristic X-rays of the sample. The X-ray signal is detected by a reverse bias *p-i-n* type lithium drifted silicon detector. The detector was mounted at a take-off angle off 37.5° to the sample surface in order to obtain the optimum X-ray yield without interfering with the objective lens. Using lower take-off angles reduces the X-ray yield as they are absorbed by passing through more material in the sample. The detector has a resolution of 10eV quoted by the manufacturer and measurements were set with an acquisition time of 30 seconds in order to prevent the Aluminium K and Silicon K peaks from converging due to increasing counts of fluorescent X-rays being detected. Thermo Scientific NORAN Microanalysis (NSS) software was used initially to calculate the composition of the samples however due to unexpected results early in the project the STRATAGem software package was used and will be discussed in section 3.4.2.

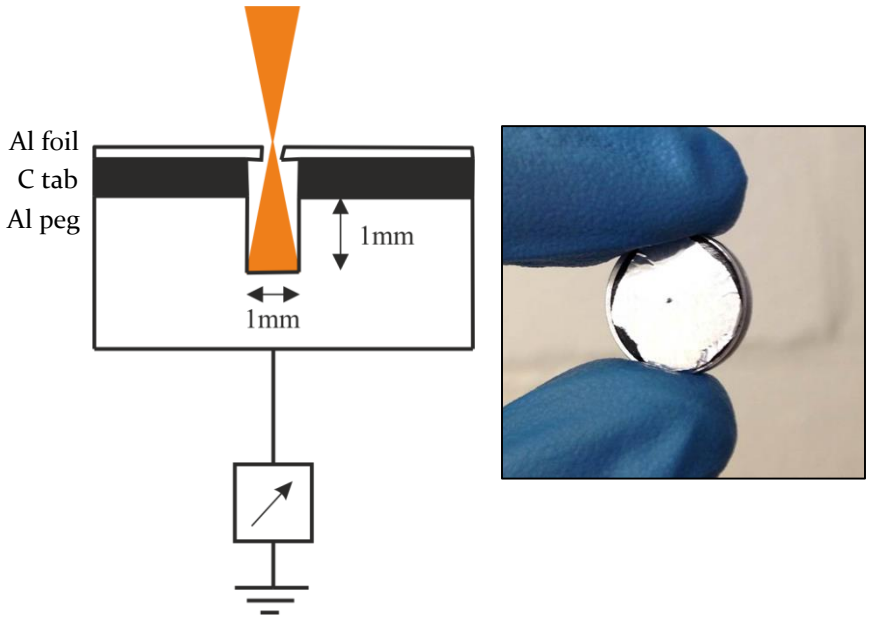

Figure 3.10: A schematic and photograph of the Faraday pot made for this project.

The beam current was measured by mounting a Faraday cup in one of the sample stage positions and connecting it to a picoammeter. The device operates by capturing the electron beam which in turn charges the walls of the cup and generates a current. The output signal described by:

$$I_{Fara} = \frac{N_i e}{t} \tag{3.8}$$

where N_i is the number of ions observed in a time t, I_{Fara} is the measured current and e is the electronic charge. A measured current of one nanoampere corresponds to around 6 billion

electrons striking the walls of the cup every second. In order to create the cup an aluminium peg with an adhesive carbon coating was drilled to have a 1mm x 1mm hole in the centre. The peg was then covered in aluminium foil which was gently pin pricked to create the structure described in figure 3.10. This technique allows the beam current to be measured directly and is independent of factors such as the resistance and structure of the samples. This is important as the energy density of the beam must be known for quantitive EDS analysis. Typically, I_{Fara} was in the range of 1 to 3nA

3.4.2 Optimising microanalysis for Heusler alloy thin films

Measuring thin films accurately using EDS is often difficult because the interaction depth of the electron beam is greater than the thickness of the thin film. For example by using the Monte-Carlo based simulation package CASINO it was calculated that an electron beam accelerated at 8keV will penetrate around 800nm into the samples [87]. As the films were grown at a thickness of 100nm for EDS analysis, around 80% of the X-rays are produced from the Silicon substrate. Figure 3.10 shows another challenge in measuring the Heusler Alloy thin films because the Aluminium and Silicon K-peak energies are similar. This means that a high signal to noise ratio must be achieved in order to have a well-defined Aluminium peak for optimal analysis. The difficulty of measuring light elements such as aluminium using EDS is well documented [88, 89, 90]. This is because light elements have a characteristically low X-ray yield due to the core levels relaxing by Auger emission, and low energy X-rays (< 2keV) were partially absorbed by the protective Beryllium window in the spectrometer [91, 88]. In this project optimising the composition of the thin films is critical, therefore a full investigation in to optimise the SEM setup was undertaken in an attempt to make accurate direct measurements of the film compositions.

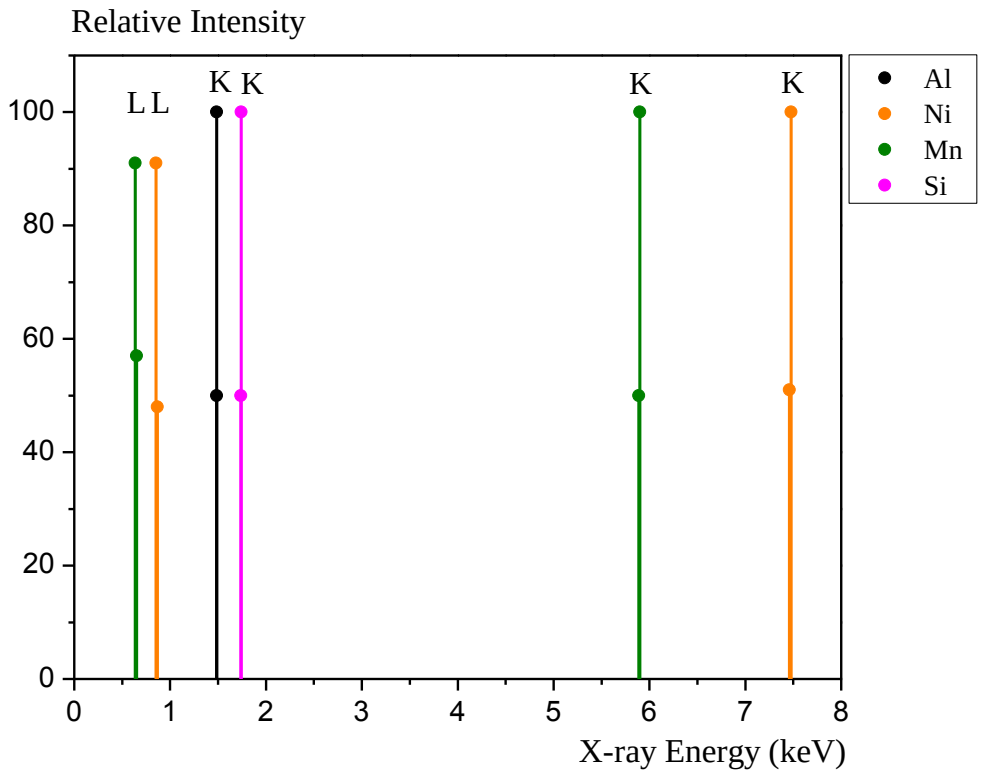

Figure 3.11: The characteristic X-ray energies of Ni_2MnAl on a Si substrate. The intensity is relative to the maximum profile for a characteristic K or L line of each element.

In order to measure accurate k-ratios (discussed fully on p.46) for thin film composition analysis the response of the bulk surface has to be carefully considered [92]. This is because low angle X-rays are absorbed as discussed in section 3.2.3. Therefore a bulk sample with a rough surface will have a different absorption co-efficient to the thin films being analysed. As such the high purity (≥99.5%) bulk samples used to calibrate the SEM were levelled and polished using a 0.1µm diamond pad to create a surface as similar to the thin film as possible. The bulk samples were cut to 1mm thickness as it is a similar thickness to the sample substrates. The bulk samples were focused in the SEM by varying the z-position of the sample stage instead of modifying the electron beam focus. This was to ensure that the energy density of the electron beam was constant throughout the measurement. The accelerating voltages used to take EDS data also had to be considered because Bethe showed that the cross section of X-ray emission is dependent on the over-voltage which is the ratio between the beam acceleration energy and the ionisation energy of an electron orbital [93]. The cross section is maximised when the accelerating voltage is approximately three times greater than the X-ray energy as shown in figure 3.12. This is due to a balance between the electrons being absorbed by the atom and the electrons being energetic enough to transverse through the atom. As a result of this, the lowest energies possible have to be used in order to maximise the signal from the Heusler alloys because the Aluminium peak is a

factor 8 lower in intensity than the transition metal peaks. Therefore measurements began at 5.08keV in order to observe all of the expected K-lines without depleting the signal from the aluminium.

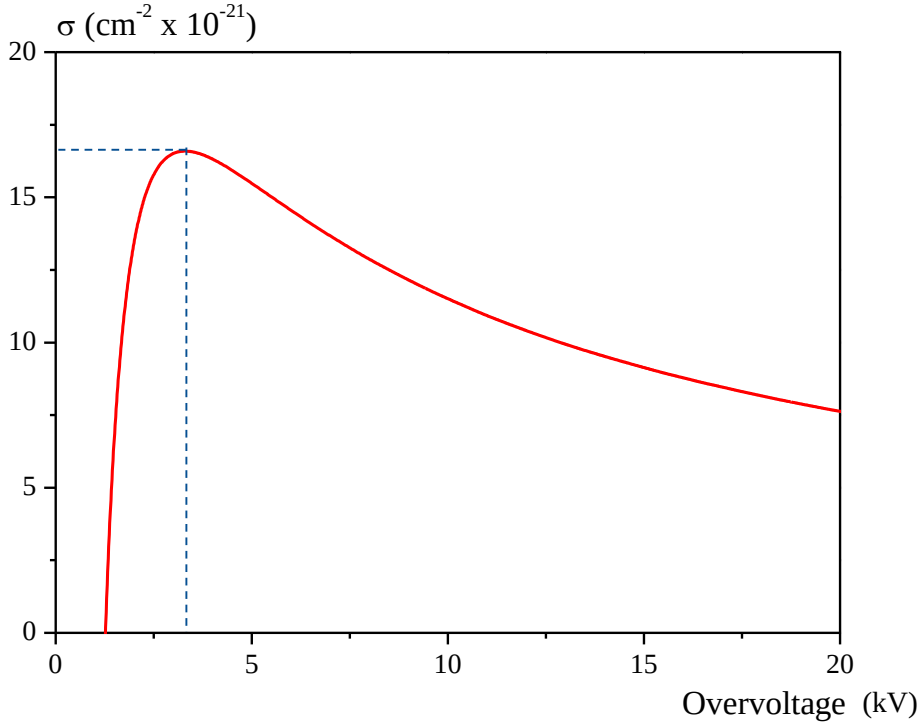

Figure 3.12: Plot of the cross section σ for inner shell ionisation as a function of overvoltage.

3.4.3 STRATAGem analysis

STRATAGem is a thin film analysis software package developed by SAMx [94]. The software operates by using the Yakowitz and Newbury method of fitting EDS data to a modelled parabolic X-ray depth production curve $\phi(\rho z)$ [95]. The curve predicts the intensity of the X-rays emitted from a thin film based on a number of physical properties; primarily the thickness and density of the film. A comprehensive discussion of the model can be found in *Goldstein 1984* [96]. STRATAGem was chosen as a potentially more accurate fitting software package with the aim of achieving measurements of the composition of the samples with a reproducibility of 5% or better. This level of accuracy was required because the lattice parameters of the Heusler alloy samples were carefully modified by doping in order to change their magnetic and crystalline properties.

STRATAGem was expected to provide more reliable data than the NSS package because it incorporates a model that is considered more physically realistic as it corrects for thin film

specimens that contain light elements in a heavy element matrix [88, 89, 90]. The STRATAGem package requires the structure of the sample to be input into the calculation in order to simulate a set of idealised results. The user must input a value of the density for the films which are listed in table 3.1 along with a thickness and composition estimation. The k-ratio which is the X-ray intensity ratio of a thin film in a substrate to bulk standard is experimentally determined by:

$$k = {}^{I_{film}}\!/_{I_{bulk}} \tag{3.9}$$

where I_{film} is the intensity of X-rays from the element in the film and I_{bulk} is the intensity of X-rays emitted from a pure bulk sample of the same element.

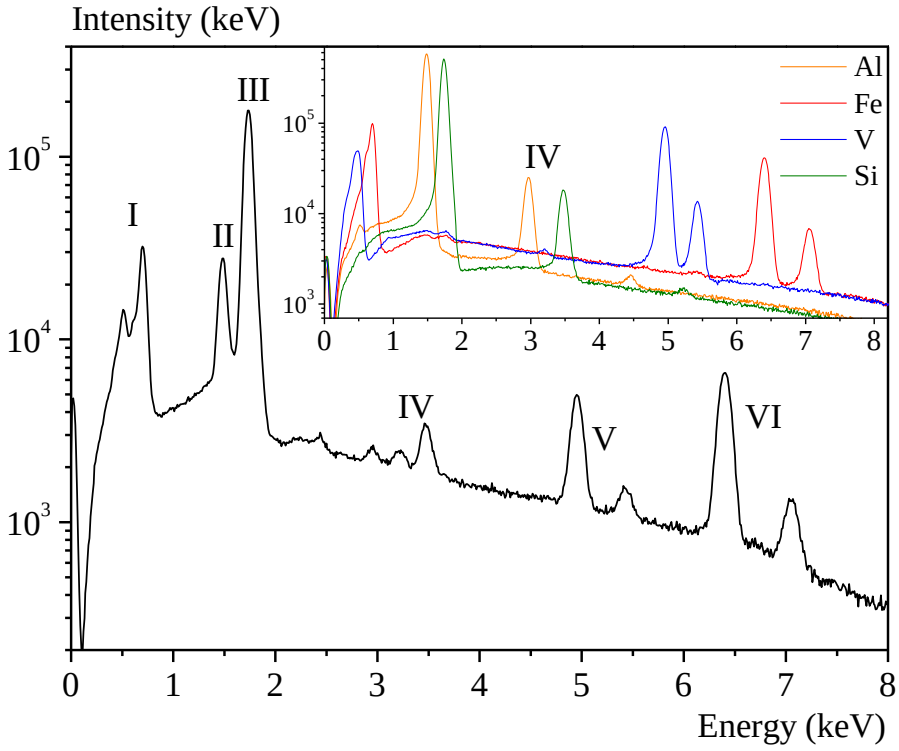

Figure 3.13: Raw EDX data from a Fe_2VAl sample measured using a 10keV electron beam. The inset shows spectra from 99.995% pure element samples under identical beam conditions in the same SEM chamber.

Figure 3.13 is a typical spectra used for measuring the *k*-ratios required for STRATAGem analysis. The intensity of the kα lines from the pure element samples was divided against the intensity of the corresponding lines from the Heusler alloy sample. The intensity of the peaks was normalised to (cps/nA) by measuring the beam current during every measurement cycle. This was

done to minimise the error in measurement intensity caused by difference experimental conditions at different electron beam energies. Once the k-ratios were determined they were input to STRATAGem for further analysis. The peaks in figure 3.13 at **I** are the Vanadium and Iron L-lines respectively. The peaks at **II** and **III** are the Aluminium and Silicon K-lines. The artefacts at **IV** are sum peaks which are caused when two or more photons are registered by the detector within a given integration time. Such peaks are also visible in the pure Aluminium and Silicon spectra in figure 3.13. This effect can be minimised by decreasing the beam current used and hence lowering the overall intensity of the measurement. The acquisition time of the measurement was set at 30 s in order to minimise any error caused by EDX artefacts. The peaks at **V** and **VI** are the Vanadium and Iron Kα and Kβ lines.

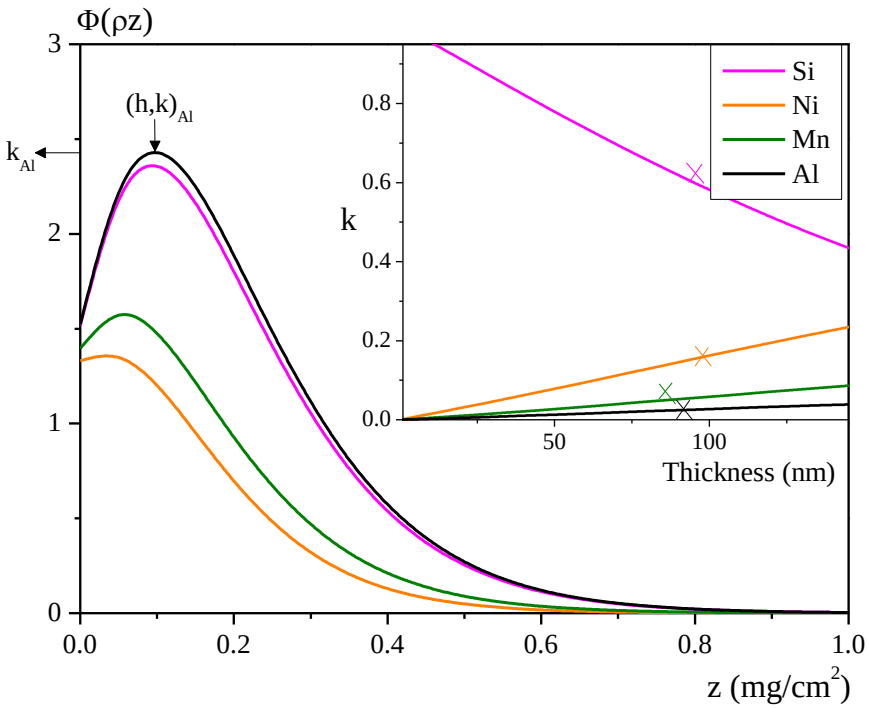

Figure 3.13: The calculated response of Ni_2MnAl under a 10keV electron beam. The insert is the software output calculation of layer thickness at different k-ratios. The data points (cross) are experimentally determined k-ratios from using an 8keV electron beam.

STRATAGem fitted the experimentally determined k-ratios for each of the element X-ray lines to calculated k-ratios using a least squares fitting technique. From fig. 3.12 the (h,k) co-ordinate describes the height of the peak top and the k-ratio for a characteristic X-ray line for a particular beam accelerating voltage. The software then calculates the film thickness by integrating over the $\phi(\rho z)$ function to calculate the k-ratios across a range of thicknesses (figure 3.12 inset) and compositions. The experimentally determined k-ratios are plotted on the $\phi(\rho z)$ vs

z graph. The software then fits the calculated curve to the experimental data points. It does this by using a calculation by *Reuter* predicting the X-ray intensity for a given bulk element [97], as a result (3.9) becomes:

$$k = \int_0^{\rho z \leq 1.5h} \varphi_{film}(\rho z) d\rho z \Big/ 0.125(\varphi_0 + 3k)(0.865(\rho z - 1.5h) + 3h) \qquad (3.10)$$

where φ_0 is the y-intercept at z = 0, h is the peak height. By using this theorem it is possible to predict the thickness of a film from the z parameter and the composition from the density parameter ρ and the expected sample stoichiometry. By measuring k at a range of different electron beam voltages (8keV – 30keV) the data was reproducible to 10% across multiple measurement positions on a sample and for a trial of 10 repeat measurements.

There were limitations to using the STRATAGem package. The primary source of error in this technique was from equation (3.10) because multiple variables were used to fit the parabolic $\phi(\rho z)$ function to the experimentally obtained *k* meaning that the fitted solution was not unique. The software assumed that the density of the films is comparable to the density of the accepted bulk values however it is known that for sputtered thin films the density is not uniform across the sample and is typically ~90% of the bulk density [58]. The values for φ_0 and *h* were highly dependent on the fitted profile which was arbitrarily tweaked by the iterative fitting procedure therefore making them unreliable. Another source of error was from the use of catalogued parameters to describe the electron scattering characteristics of a sample. STRATAGem used values measured from pure elements and combined them based on the sample stoichiometry which was unlikely to accurately describe to the scattering processes in the samples. This is because the crystal structure and composition are not uniform in the sample and therefore cannot be compared to bulk elements. Therefore although STRATAGem was a useful analysis tool for providing an indication of the sample composition, the model on which it operates was fundamentally flawed by an excess of free parameters. The software could not deliver the accuracy required for the project leading to an alternative measurement technique being used and the attempted use of EDS for a direct composition measurement being relinquished.

3.4.4. Chemical analysis

Due to the accuracy of the EDS data being unsuitable for this work samples were analysed by Intertek Ltd [11] for chemical composition analysis at ISO9001 standards. For the analysis Ni_2MnAl and Fe_2VAl samples were grown at a thickness of 100nm on glass substrates at bias voltages of 300V and 900V. One of each sample was sent to Intertek and another from the same

sputtering run was retained. This allowed for the EDS to be used as a comparator by measuring the spectra from the chemically analysed reference samples and comparing them to the samples being measured under the same beam conditions. At Intertek the samples were placed in separate sample tubes and digested using aqua regia (HCl: 15ml, HNO_3: 5ml), they were diluted to a final volume of 30ml with demineralised water. Blank glass substrates were also analysed in the case of any unexpected contaminants being measured. The solutions were then analysed using inductively coupled plasma optical emission spectroscopy (ICP-OES) [98].

ICP-OES is a comparator measurement with an accuracy of 0.1% as quoted by Intertek. The measurement works by generating an Argon plasma inside a quartz tube using a three turn Copper radio frequency transmitter [98, 99, 100]. The solution is then sprayed in to the plasma as a fine mist resulting in the ionisation of the sample within the plasma. This results in the emission of photons with energies that are characteristic to the elements within the sample. An optical chamber consisting of a diffraction grating is used to split the radiation in to its wavelength components and then analyse the intensity of the radiation using semiconductor photodetectors. The intensity of each element line is then compared to calibration curves that are generated by analysing pure samples of known concentrations. The results of the chemical analysis showed that the deposited films were within 5% of the target stoichiometry and were therefore suitable for further study. Detailed chemical analysis to measure which valence the chemicals were in was deemed unnecessary because the films had not sufficiently alloyed, the focus of the experiment was to confirm that the composition of the films was comparable to the composition of the sputtering targets.

Heusler Alloy	**Bias Voltage**	**Composition (± 0.01%)**		
X_2YZ	**V**	X	Y	Z
Ni_2MnAl	900	53.32	26.29	20.39
Ni_2MnAl	300	50.94	26.89	22.17
Fe_2VAl	900	53.75	20.09	26.16
Fe_2VAl	300	55.25	16.53	28.22

Table 3.3: The results of the chemical analysis performed by Intertek.

Chapter 4: Results and Discussion

4.1 The crystallisation of Heusler alloy thin films

The main objective of this work was to map how a range of Heusler alloys crystallise under different annealing conditions. The thin films were annealed *ex situ* for up to six hours in one hour or thirty minute intervals at temperatures in the range of 200°C to 800°C. The films were then characterised in between each interval of annealing by the use of X-ray diffraction scans. The quality of the crystallisation of the samples was quantified by measuring the Q factor of the Heusler alloy (220) peak. The Q factor was measured as the intensity of the peak (counts per second/degree) divided by the full width half maximum of the peak. This meant that the observations of broad peaks lead to the interpretation of there being several grains that were out of alignment from the surface normal of the thin films. An increase in the Q factor described an increased presence of grains within the thin films as well as a change in the texture of the film from a number of disorientated grains to the development of a partially ordered set of grains with a columnar texture.

4.1.1 The crystallisation Ni_2MnAl

The Ni_2MnAl samples were annealed for up to six hours at temperatures in the range 250°C to 700°C. There was no crystallisation observed in any of the samples that had been annealed at a temperature below 700°C. The presence of a small number of A2 ordered nanocrystals was indicated in all of the as-deposited samples by a weak (220) Heusler alloy peak at 44.0° with a FWHM of 0.7° as shown in figure 4.1. The FWHM of the rocking curves that were used to measure the texture of the (220) peak indicated that the as-deposited grains were aligned ±15° from the sample surface. A series of pole figure scans about the positions of the Heusler

alloy (200) and (111) peaks suggested that the nanocrystals were ordered in the A2 phase because no extra peaks were observed. The lattice parameter could not be determined accurately from the as-deposited scans because of the low intensity and broad profile of the peak.

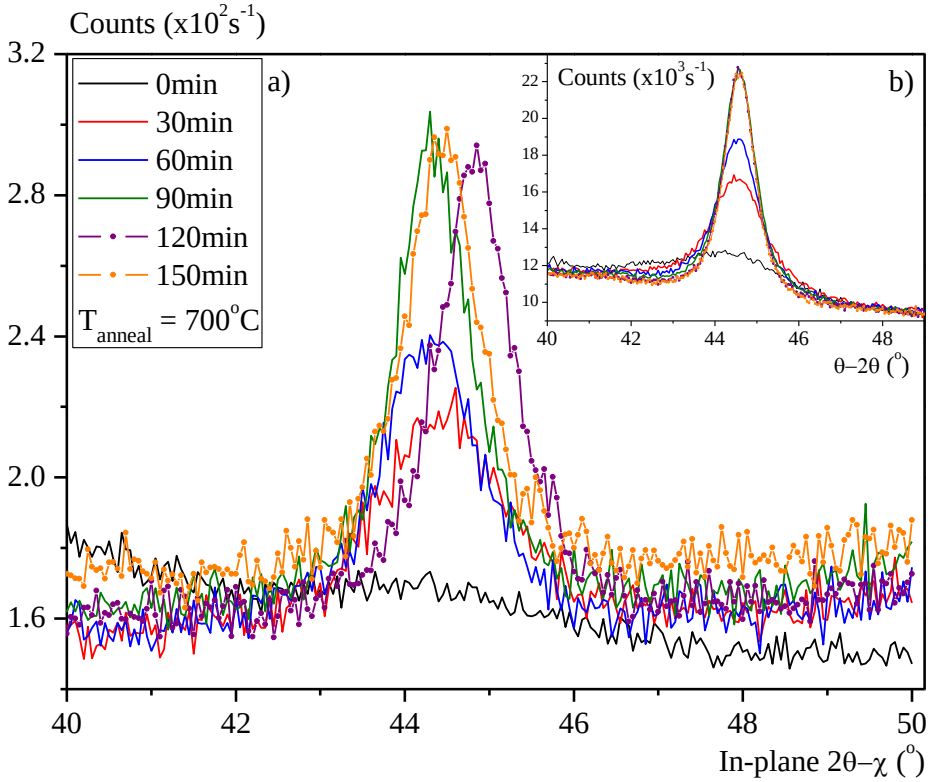

Figure 4.1: The growth of the Ni_2MnAl (220) peak measured in a) in-plane and b) out of plane scan geometries.

The Ni_2MnAl samples were measured with a grazing incidence $\theta = 0.4^o$. $2\theta\chi$ refers to the 2θ detector arm sweeping in the plane of the sample (χ). This means that 'out of plane' refers to the diffractometer geometry scanning in q_z and 'in-plane' refers to the diffractometer geometry scanning in q_x. The (220) peak began to grow once samples were annealed at 700°C as shown in figure 4.1. A well-defined (220) peak developed out of plane within the first 90 minutes of annealing. However after annealing for a further 60 minutes no further out of plane crystallisation was observed as shown in figure 4.1 b). The lattice constant of Ni_2MnAl was measured as (5.753 ± 0.001) Å from the out of plane peaks. There was a transition in the in-plane (220) peak when the sample was annealed for more than 90 minutes. The transition corresponded to a 1% change in the in-plane lattice constant from (5.77 ± 0.01)Å to (5.71 ± 0.01)Å. There were no observations of the (200) or (111) peaks in the sample which suggested that the transition in the (220) peak was not indicative of a phase transition. The larger error quoted in the measurement of the in-plane lattice constant was due to the weaker signal associated with the in-plane scanning geometry

making the peaks more difficult to quantify. The scan times had to be limited to one hour as a high throughput of samples and measurements was required for the HARFIR project.

The unknown phase change could have been caused by relief of the strain in the lattice that was induced by the annealing process. Another possible explanation is diffusion from the Silicon substrate in to the sample as a result of the high temperature of the annealing. The X-ray scanning geometries must be discussed in order to interpret figure 4.1 in the context of Silicon diffusion and relaxation of to the sample. The penetration depth of the fixed grazing incident angle is likely to have been less than the 100nm of Heusler alloy as no Silicon substrate peaks were observed using this geometry. The out of plane geometry is not sensitive to diffusion at the interface because it is measuring the q_z spacing of the layers which is likely to be relaxed as crystallites grow. When the sample is observed in-plane the geometry is sensitive to the q_x lattice spacing of the layers. Diffusion and strain are easier to see in this configuration because this is the plane of the interface where the lattice of the Heusler alloy is strained to the lattice of the substrate. This could be why the (220) peak is shifting in figure 4.1 a) and not in figure 4.1 b). For example a possible reason for the translation occurring after 90 minutes is that it was initially more energetically favourable for grains of Ni_2MnAl to grow in the q_z direction through the thickness of the film. Then after 90minutes the Ni_2MnAl grains began to in the q_x direction through the plane of the film where the interface could be affecting the crystallisation process. This could explain why there is an initial growth of the (220) peak which stops in the out of plane direction whilst the in-plane direction grows and translates.

Annealing time	**Q Factor (±0.1)**		**Lattice constant**	
(hours)	**OP**	**IP**	**OP (±0.01Å)**	**IP (±0.01Å)**
0.5	434.2	68.2	5.76	5.73
1.0	985.0	79.1	5.76	5.75
1.5	1203.1	84.2	5.75	5.77
2.0	1192.3	94.4	5.75	5.71
2.5	1185.1	120.6	5.75	5.76

Table 4.1: The out of plane q_z (OP) and in plane q_x (IP) lattice constants of A2 ordered Ni_2MnAl as calculated from the (220) peak for samples annealed at 700°C.

4.1.2 The growth of Ni_2MnAl on Silver

The crystallisation of Ni_2MnAl when grown on a seed layer was studied in an attempt to assist the crystallisation of the thin films. The samples were measured using the standard θ-2θ X-

ray geometry to ensure that both the Silver and Heusler alloy layers were being measured. The high annealing temperature of Ni_2MnAl was unsuitable for device applications because there would be a considerable amount of diffusion between any multilayers in the devices. The use of a seed layer was predicted to lower the ordering energy of the Ni_2MnAl in the local environment. Therefore the film was expected to have an A2 ordered lattice as deposited. The A2 to B2 phase transition temperature of the ordered film may then been lower, however no publications could be found to validate the hypothesis. Figure 4.2 shows the resulting out of plane X-ray scans of Ni_2MnAl samples grown on Silver at a variety of thicknesses. The difference in the noise base of the scans was due to the alignment of the sample z-position finishing at slightly different positions within the X-ray beam. The sharp peak at 33° is from the Silicon substrate whereupon the small diffraction fringes were observed about the position was due to the X-ray beam not being perfectly aligned to the substrate.

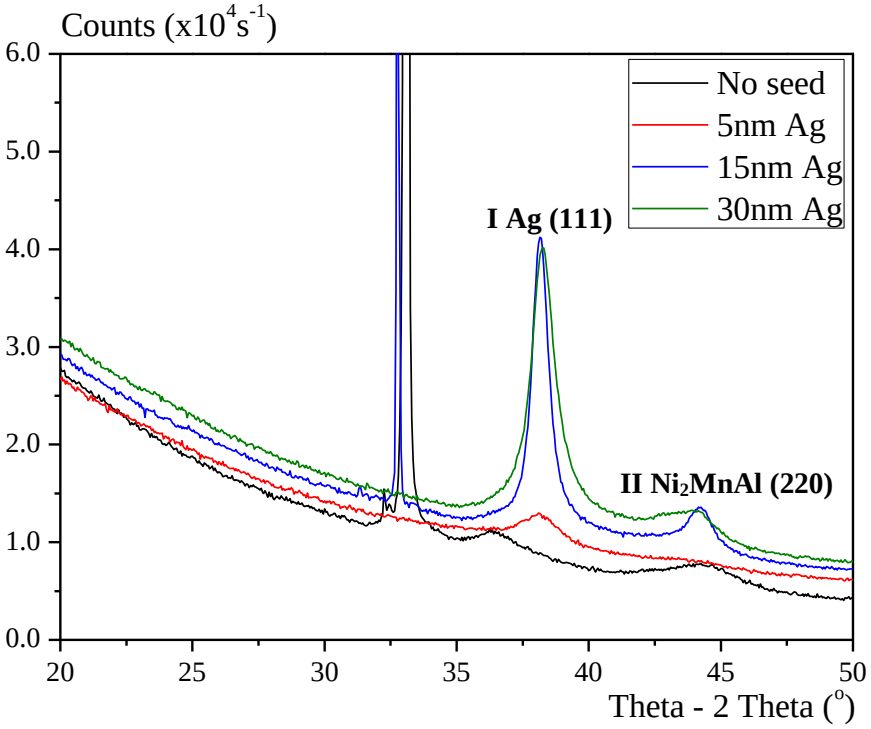

Figure 4.2: The crystallisation of Ni_2MnAl as deposited on Silver.

Silver was chosen as a suitable seed layer because the lattice mismatch was calculated to be 0.01% when the crystals were oriented at 45° to the Ni_2MnAl. The Ni_2MnAl layer was grown to a thickness of 20nm in order to be representative of any future device structures. The peak observed at 36° from the as deposited sample is potentially the Aluminium (111) peak. The peak at **I** was identified as the Silver (111) peak. The interpretation of **I** was aided by cross sectional TEM images by *Sagar* [54]. At a thickness of 5nm the Silver was weakly ordered as demonstrated

by a Q of 1 x 10^3 which suggested that the layer was crystalline. The peak at **II** is the Ni_2MnAl (220) peak which was not observed when the Ni_2MnAl was grown on top of 5nm of Silver. The Q of the Silver (111) peak became 3.0 x 10^5 when the Silver layer thickness was 15nm which suggested that the layer was highly ordered. This was supported by a sharp Ni_2MnAl peak which suggested that well-ordered A2-phase grains were grown. The broadening of **I** was encompassed a change in its Q to 1.8 x 10^5 which was indicative of an increase in the crystallinity of the Silver layer when the thickness of the layer was 30nm. This was supported by the images reported by *Sagar* [54] whereupon the crystalline 'clusters' were successfully imaged. The uneven structure of the 'clusters' is likely to have reduced the effectiveness of the seed layer which was demonstrated by a broadening of the Ni_2MnAl (220) peak suggesting a decrease in the diameter of the Heusler alloy grains. The Q of the as deposited Ni_2MnAl increased from 210 to 3230 when a seed layer was used which indicated that Silver is an effective seed layer for the growth of Ni_2MnAl when the layer thickness is 15nm.

4.1.3 The crystallisation of Fe_2VAl

The Fe_2VAl films were annealed for up to six hours at temperatures in the range 250ºC to 700ºC. Figure 4.3 describes the amount of A2 ordering observed in the samples based on the Q factor of the Fe_2VAl (220) peak. The largest Q factor of around 200 describes a sharp in-plane (220) peak that is indicative of a good degree of crystal ordering when compared to the Ni_2MnAl samples which had an in-plane Q factor of around 100. The measurement was conducted on Fe_2VAl films that were grown on 5mm x 5mm Silicon substrates whereas the Ni_2MnAl measurements were conducted on 16mm x 16mm Silicon substrates to maximise the X-ray yield. The Q factors quoted for the Fe_2VAl samples have been corrected by multiplying them by a factor of 2.5 in order to correct for using smaller substrates at the very start of the project. This factor was determined experimentally by conducting a comparator measurement on 16mm x 16mm wafers for samples annealed for 3 or 6 hours at 300ºC, 500ºC or 700ºC. The resulting Q factors were plotted against the measured Q factors from films sputtered on 5mm x 5mm substrates to create a calibration curve. The increase in the measured Q factor was found to scale proportionally to the area of the X-ray beam used to measure the samples.

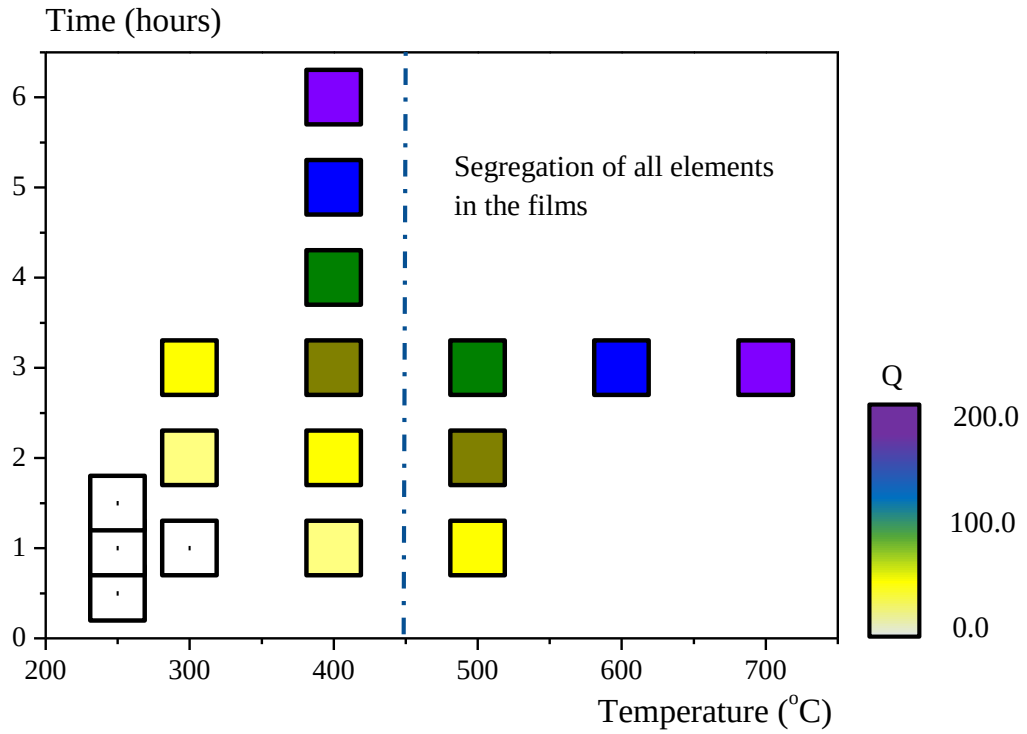

Figure 4.3: The in-plane crystallisation of Fe_2VAl thin films of 100nm thickness under different annealing conditions. The coloured tiles describe A2 crystallisation.

The Fe_2VAl thin films exhibited A2 ordering when annealed at temperatures of 300°C and 400°C. This suggests that the ordering temperature of Fe_2VAl is above 300°C because no crystallisation was observed when the samples were annealed at 250°C. The height and area of the (220) peak did not grow linearly when the samples were annealed. The intensity of the (220) peak decreased slightly on alternating annealing periods which suggested that the film could have been crystallising via a process of nucleation and recrystallisation. The intensity of the background noise had a deviation of 10% across the measurements which was less than the decline in intensity of the (220) peak which followed alternating annealing sessions. The degree of ordering was considered to be strong after annealing the samples for six hours at 400°C. This was because the intensity of the Fe_2VAl (220) peak was greater than that of the Ni_2MnAl (220) peak by around a factor of 4 when identical scan geometries were used. The mean lattice constant of Fe_2VAl was calculated to be (5.83 ± 0.03)Å from the measured (220) peaks that are listed in table 4.2. The error may have arisen from the unknown phases of the Heusler alloy being observed in the samples that were annealed at temperatures above 400°C. The (220) peak of the sample that was annealed at 700°C was not used in the calculation of the lattice constant because there was a

large amount of segregation of the elements in the thin film. There was no crystallisation observed in the 'as deposited' samples.

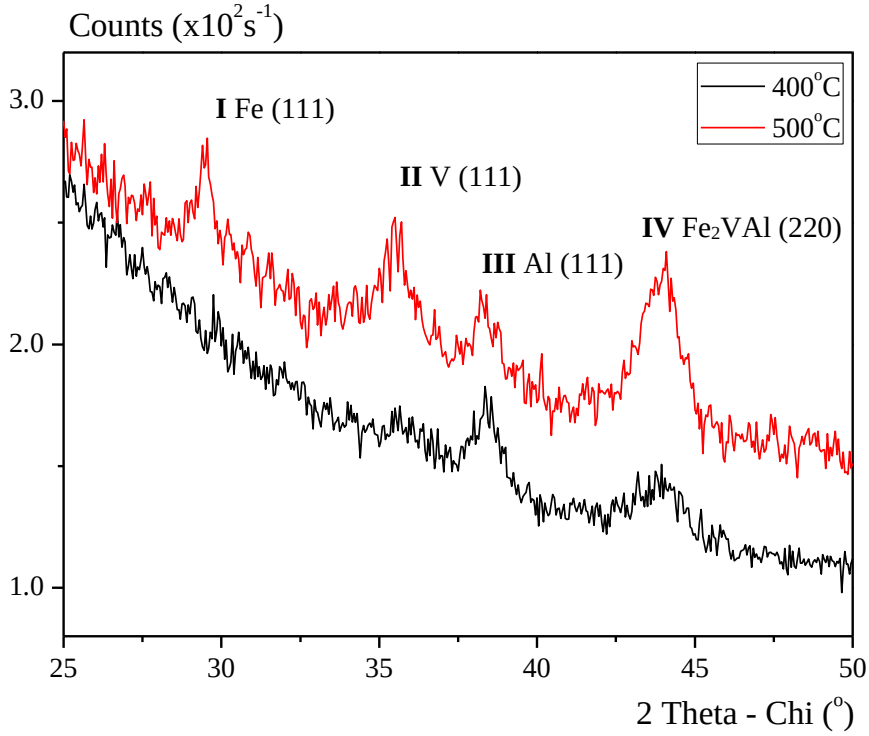

Figure 4.4: The segregation of elements from the Fe_2VAl matrix after three hours of annealing.

Segregation of individual elements was observed in the Fe_2VAl samples. This became prominent when the films were annealed at temperatures above 400°C. Peaks **I**, **II** and **III** in figure 4.4 correspond to the (111) peaks of Iron, Vanadium and Aluminium respectively. Both **III** and **IV** were observed in the sample annealed at 400°C which suggested that the lighter elements were able to segregate at lower energies.The difference in the background noise in figure 4.4 was due to the samples being at a slightly different heights within the X-ray beam. The A2 ordering continued whilst the individual elements were segregating. This could be due to the composition of the sample being inhomogenous. Segregation was not observed on this scale in the other Heusler compounds studied. The Heusler alloy thin films were all fabricated via the same process and are believed to have similar variations in their composition. Therefore the inhomogeniety of the sample composition is unlikely to be a sufficient explaination of the combined growith of Heusler alloy and pure element grains within the same matrix. Another possible explaination is that the formation energy of the Heusler alloy and pure crystal grains are similar in magnitude. Therefore the growth of a particular grain would be dependent on the local conditions such as composition and strain.

Annealing Temperature (ºC)	(220) peak Q (±0.1)	Lattice Constant (±0.01Å)
300	25.6	5.84
400	50.7	5.84
500	124.1	5.79
600	170.1	5.80
700	221.2	5.92

Table 4.2: The lattice constant of Fe_2VAl after three hours of annealing.

4.2 Magnetic characterisation of Heusler alloy thin films

The magnetic properties of the Heusler alloy thin films were measured using the AGFM in order to study how the crystal structure of the films affected their magnetic properties. The main objective of the magnetic measurements was to identify any ordered phases that had the potential to be antiferromagnetic in preparation for the fabrication of devices. The hysteresis of the sample was expressed as the magnetic moment of the sample as a function of the applied field. This is because calculating the magnetisation of the sample (moment per unit volume) was difficult as the volume of a thin film was difficult to determine. This is because the area of the thin films were measured using an optical microscope however there was a large random error in the measurement of the area was due to the edges of the thin film being hard to identify. This was because the film became transparent as the thickness of the film tapered toward its edges. The thickness of the film was read from the deposition monitor during growth which had an accuracy of 10% based on the earlier calibration test comparing with results from XRR and SEM experiments. As a result of the difficulty to determine sample area it was considered more accurate to discuss the magnetic response of the samples in the context of their magnetic moment because they were all grown on pre-cut substrates with non-identical sputtering mask areas.

4.2.1 The magnetic properties of Ni_2MnAl

There was no crystallisation observed in the Ni_2MnAl samples that had been annealed at temperatures less than 700ºC as discussed in section 4.1. Therefore the magnetic characterisation of the samples was used in an attempt to observe any changes in the samples via changes in their magnetic ordering. Little change in the magnetic response of the samples was expected because no magnetic ordering was thought to have taken place. The magnetic properties of $L2_1$ ordered

and B2 ordered Ni_2MnAl have been predicted to be ferromagnetic and antiferromagnetic respectively [41]. Therefore the measured magnetic response of the thin films could have indicated whether any crystallisation was occurring at a scale that was below the resolution of the X-ray diffractometer. Any unexpected magnetic response could also have provided some insight into any impurities or defects being present in the sample that would have led to the unfavourable ferromagnetic state to be observed.

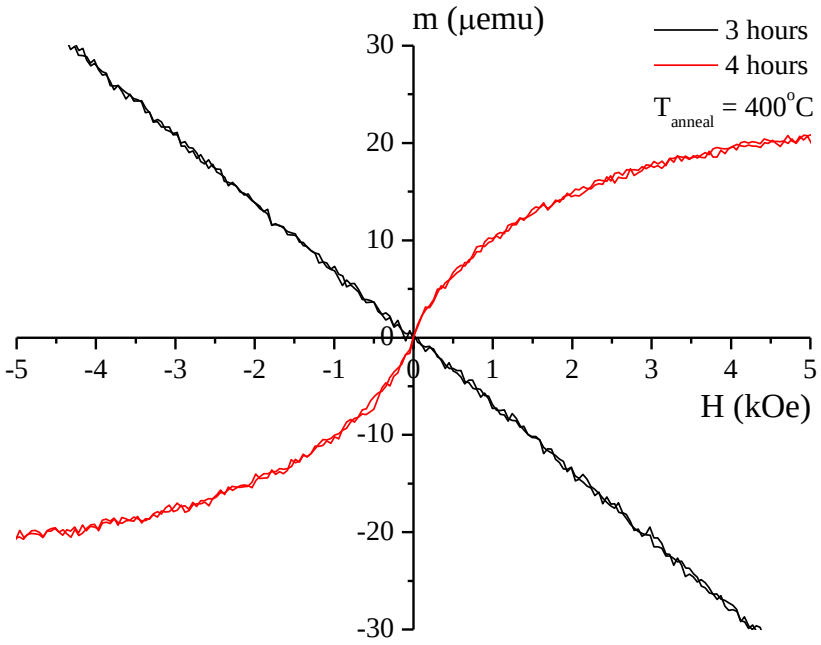

Figure 4.5: The magnetic response of Ni_2MnAl.

Figure 4.5 shows the typical response of Ni_2MnAl when annealed at 400°C. The diamagnetic response of the Silicon substrate has not been subtracted from the curve. Therefore there was no magnetic response observed from the films that were annealed for up to three hours at temperatures of up to 400°C. This means that the Ni_2MnAl could potentially have been antiferromagnetically ordered however this is unlikely because of the low degree of crystallinity observed in the samples. The samples exhibited a superparamagnetic response when annealed for over 4 hours or at temperatures exceeding 400°C. The magnetic moment of the samples was typically 20 - 40μemu and the coercivity was measured to be in the range of 0 – 20Oe following the subtraction of the magnetic response of the substrate as measured before sputtering. The sudden change in response shown in figure 4.5 was initially treated as possible contamination of the sample or the probe. Films from a separate sputtering session were annealed under the same conditions and were found to have similar properties. It is possible that the annealing process lead to diffusion within the amorphous film which could have caused Nickel nanocrystals to develop. No evidence of Nickel ordering was observed in the X-ray scans and it is likely that any

nanocrystals would be too small or too low in concentration to detect. This is supported by the low saturation magnetisation of the film. The samples that were annealed at 700°C and the samples that were grown on a Silver seed layer exhibited superparamagnetic behaviour. The data for films grown on Silver has been omitted as the HARFIR project is focused on engineering antiferromagnetic films only.

4.2.2 The magnetic properties of Fe_2VAl

The Fe_2VAl thin films were characterised magnetically to evaluate how the magnetic ordering changed in relation to the crystallisation of the thin films. The films were successfully crystallised when annealed at temperatures between 300°C and 400°C for up to 6 hours as discussed in section 4.1.3. Crystallisation of the thin films was observed in all samples that were annealed at temperatures over 400°C for three hours however multiple phases of pure-element and Heusler alloy grains were observed. This meant that the magnetic measurements would describe a combination of grains made of either Fe_2VAl, Iron or any unknown alloys that were present. The films were expected to behave ferromagnetically because Fe_2VAl is a well-known ferromagnet whose antiferromagnetic state is predicted to depend critically on the composition of the material which should be close to $Fe_{2.5}V_{0.5}Al$ [29]. Therefore an increase in the crystallinity of the thin film should have led to an increase in the magnetic moment of the sample as more Iron sites were able to couple magnetically. This gave another observation of the quality of the crystal ordering which was useful for supporting the X-ray diffraction measurements.

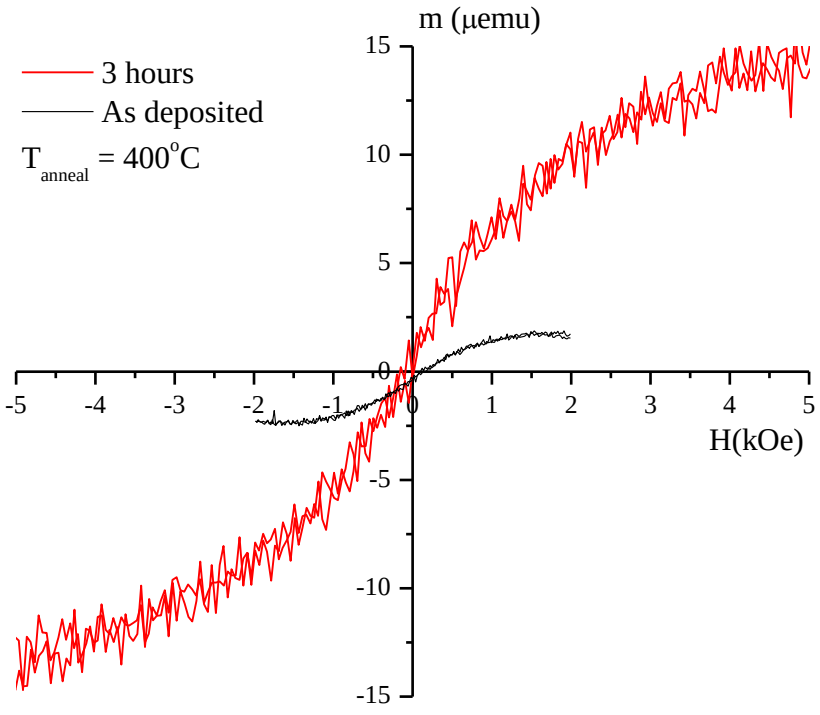

Figure 4.6: The magnetic response of Fe_2VAl before and after annealing.

The Fe_2VAl thin films exhibited superparamagnetic behaviour in the as-deposited state. The saturation magnetisation of the samples increased monotonically with annealing time and annealing temperature. Figure 4.6 is a comparison between the magnetic response of a Fe_2VAl film before and after three hours of annealing at 400ºC. The increased noise for the later measurement is most likely due to damage to the AGFM probe as the devices are fragile and shared amongst several users. The saturation field of the sample increased from 1.5kOe to 7.5kOe and the saturation moment increased from 2μemu to 15μemu. The increased superparamagnetic response of the thin films could have been caused by disordered crystal grains forming. The Iron (111) peak was observed in all samples that were annealed when the integration time of the X-ray scans was doubled. This suggested that it could be favourable for small Iron crystallites to aggregate within the film during the annealing procedure. The superparamagnetic response could alternatively be due to the stoichiometry of the samples not being $Fe_{2.5}V_{0.5}Al$. This is because a higher Iron concentration is required to strain the lattice to allow quasi-free Iron ions to couple antiferromagnetically [29]. The moment of the films would reduce with further annealing if this was indeed occurring however as the opposite is true is can be inferred that the films are not of the correct composition for antiferromagnetic order.

4.2.3 The magnetic properties of exchange coupled bilayers

A series of bilayer structures were grown as an exercise to see whether any exchange coupling was possible using Ni_2MnAl films that had an optimised growth procedure as an antiferromagnetic layer. The films were grown on a 20nm Silver seed layer with a 20nm Ni_2MnAl layer and a 5nm Co_2FeSi layer. The dimensions of the bilayer were designed to imitate an exchange biased device [101]. The films were deposited using HiTUS steering bias voltages from 300V – 900V and capped with an amorphous layer of Tantalum to protect the samples against corrosion. The aim was to crystallise the Ni_2MnAl in the antiferromagnetic B2 phase by using a seed layer and a slow deposition rate. Co_2FeSi was chosen as the ferromagnetic layer because it has an almost perfect lattice match to the Ni_2MnAl and it was known to crystallise at 250ºC [55]. Successful coupling of the two Heusler alloy layers would have been novel and a good foundation for further research. The films were annealed at 100ºC for 10 minutes prior to each measurement in the VSM in order to orient the order of any antiferromagnetic grains that could have been present. The annealing conditions quoted in figure 4.7 describe the settings used in the furnace before measuring the sample.

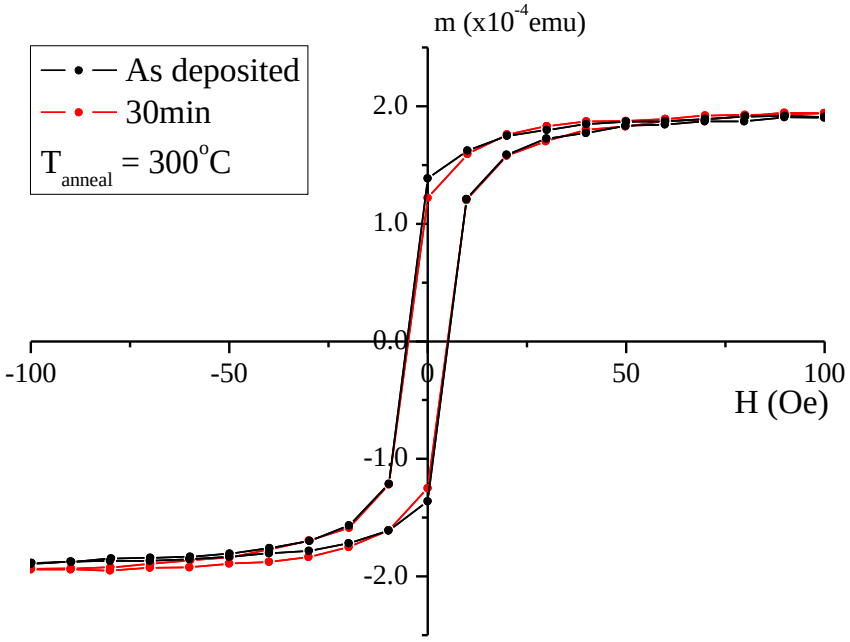

Figure 4.7: The magnetic response of a Ni_2MnAl and Co_2FeSi bilayer.

The hysteresis of the samples was measured at a temperature of 77K in order to minimise the probability of thermal energy in the lattice disorienting any antiferromagnetic domains. Figure 4.7 shows the typical magnetic response of the samples whereupon no exchange coupling was observed. The magnetic moment of the samples had a variation of ~5% when the samples were grown at different bias voltages which suggested that there had been little change in the crystal structure. The magnetic moment of the samples also showed little change after annealing which was unexpected because the magnetic moment of the ferromagnetic Co_2FeSi should have increased with further annealing at 300°C and corresponding crystallisation [55]. This suggests that there could have been diffusion between the layers which was more energetically favourable than further crystallisation of the samples.

4.3 EDS optimisation for Heusler alloy thin films

Measurements of the composition of the first batch of samples were neither reproducible nor comparable with the expected results. Repeat measurements across a sample during the same measurement yielded a variation of the measured composition of up to 20%. This was unsuitable for the level of accuracy required for the work and lead to the challenges discussed in section 3.4.2 being identified. An investigation into the operating parameters of the SEM was also begun so that future measurements were reproducible and therefore comparable for different samples. One aim was to minimise the overlap between the K_α and K_β peaks of the light elements so that the signal from the thin film could be distinguished from that from the substrate. This was

achievable by maximising the electron yield per unit time so that well defined peaks could be measured within a short measurement time before fluorescent X-rays broadened the peaks and increased the noise base. Another aim was to standardise the procedure in which the measurement was taken so that raw data such as the intensity of the peaks was comparable between measurements.

4.3.1. Optimising the Electron Beam Parameters

The optimisation of the electron beam parameters was the most convenient way to maximise the X-ray yield required to obtain well defined spectral lines. There were several settings of the instrument that were constrained, for example the mechanical aperture, because the SEM was a general use instrument that was maintained by a technician. Users were only permitted to vary the spot size and acceleration voltage in order to prevent any misalignment of the electron beam during a seven day period. The electron gun tilt could also be varied slightly to improve the contrast in the image however it was not a discrete setting. The EDS detector had a limit called the dead time (DT) which was a limitation of the amount of X-rays that could be counted per unit time. The dead time limit was set by the processing capability of both the software and hardware used to count the X-rays emitted by the sample. Therefore optimisation of the electron beam parameters was a balance of maximising the electron count per unit time to prevent spectral artefacts appearing that were results of X-rays being counted incorrectly. Figure 4.8 shows the result of varying the electron beam spot size independently and the acceleration voltage.

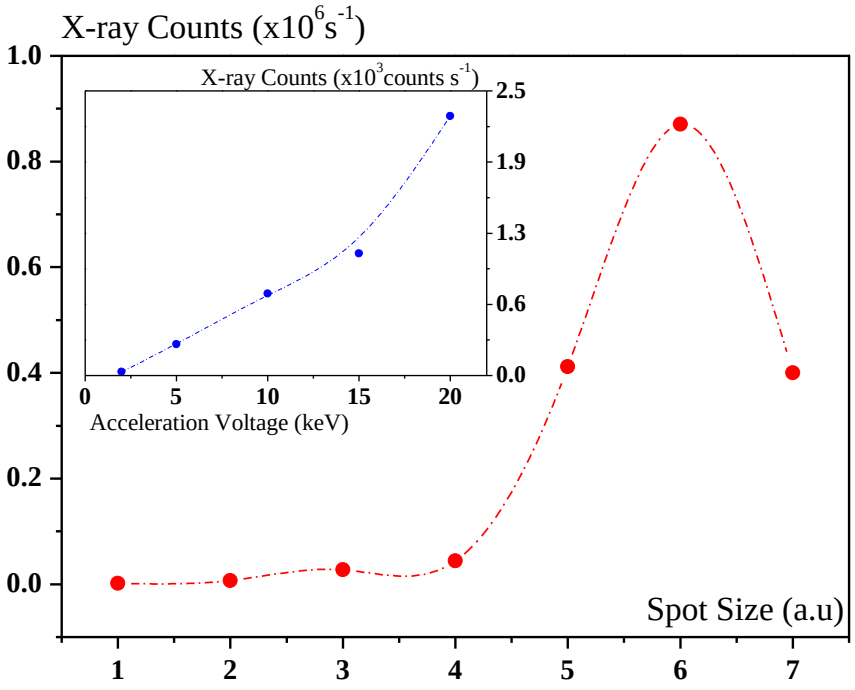

Figure 4.8: Changing EDS signal of the Iron Kα line from a Fe_2VAl film by increasing the SEM beam spot size (red) and acceleration voltage (blue inset).

A number of SEM instrument parameters were tested in order to optimise the experiment for the measurement of Heusler alloy thin films. The spot size and acceleration voltage could be controlled easily from the microscope user interface. The experiments were performed directly after the weekly beam realignment which was performed by a technician. This ensured that all beam alignment parameters were consistent for all measurements. Increasing the energy of the electron beam increased the electron yield because the interaction volume within the sample was increased. The spot size setting controlled the focus of the condenser lens. Increasing the spot size increased the electron flux through the mechanical aperture in the SEM column however it was not physically quantified. Two trends were observed whilst increasing the spot size: increasing the spot size from setting 1 to setting 4 increased the electron yield by a factor of 3; increasing from setting 4 to setting 5 increased the yield by a factor of 10 and from setting 4 to setting 6 a factor of 20. An increase of the electron yield by a factor 30 was expected when increasing the spot size from 4 to 7 however due to the extremity of the setting, all attempts at aligning the column well enough to observe this effect were unsuccessful. As the spot size settings are not physically defined it was considered that settings 1 to 4 are for fine tuning low yields of electron flux and settings 5 to 7 are for course tuning of high yields. The thin films were not damaged by the high electron flux so spot size 6 was selected for future measurements. This resulted in a beam current of 1.0 to 3.0nA being measured through the Faraday cup depending on the acceleration voltage as discussed in 3.4.1.

4.3.2 Understanding the effects of increasing acceleration voltage

A change in the spectra of the samples was observed when the acceleration voltage was changed as part of the investigation discussed in section 4.3.1. The intensity of the low energy peaks typically reduced when a larger acceleration voltage was used. This led to the investigation of how the electron beam acceleration voltage affected the measured X-ray spectra of the samples. A change in the relative intensity of the peaks would indicate a change in the composition of the sample that was calculated by the EDS control software. Figure 4.9 shows how the X-ray spectra varied as the acceleration voltage was increased.

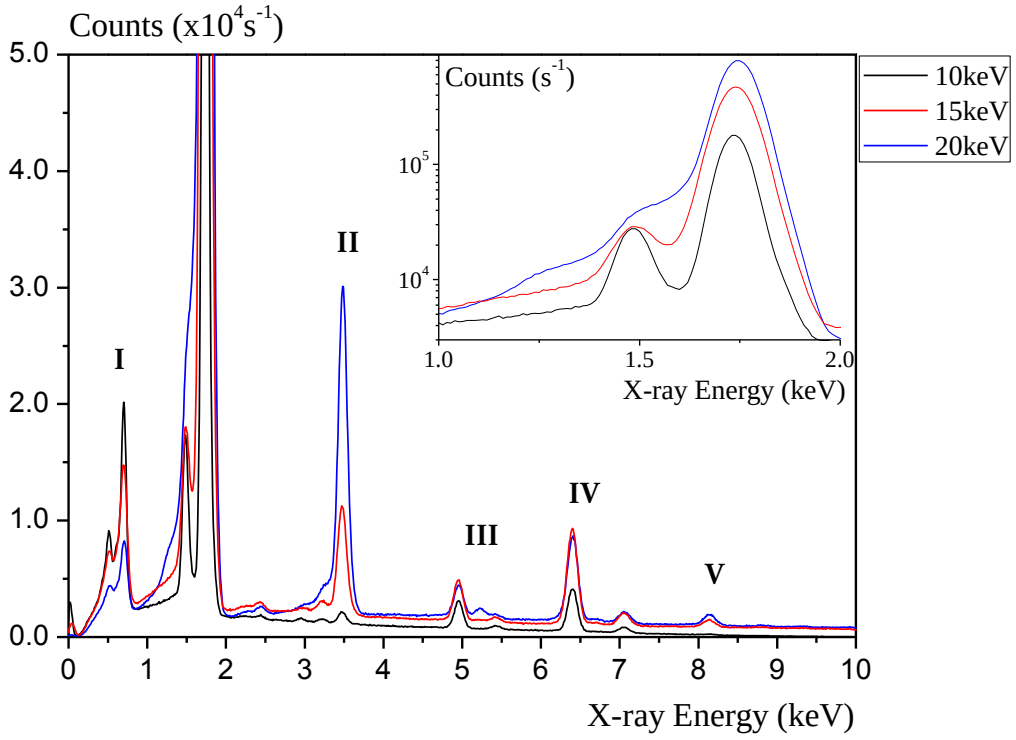

Figure 4.9: Fe_2VAl X-ray spectra, inset: the Aluminium and Silicon K lines on a log scale for clarity.

The reproducibility of the STRATAGem [81] analysis technique used to process the spectra was increased when a sample was mapped across several acceleration voltages. Figure 4.9 shows the effects of increasing the acceleration voltage from 10keV to 20keV. The lowest acceleration voltage that could be used was 8keV in order to capture all of the K-lines within the Heusler alloy. The physical manifestation of the overvoltage ratio can be observed at **I** where the low energy L-peaks of Iron and Vanadium decrease as the overvoltage ratio increases from around 20 to 40. The effect is observed again at **III** and **IV** where the K-peak counts of Iron and Vanadium increase as the overvoltage ratio approaches the optimum value of 3. Therefore for high accelerating voltages the accuracy of measuring transition metals was increased. This is because

the error associated with profiling the peaks was greater when the peak top is closer to the noise base. The accuracy of measuring the K-ratios of Iron and Vanadium was improved by a factor 10 when the accelerating voltage was increased from 10keV to 20keV.

Increasing the acceleration voltage impacted the measurement of the Aluminium K peak as shown by the insert of figure 4.9. The loss of the peak definition can be attributed to a combination of a large overvoltage ratio and an increase of fluorescent X-rays from the Silicon substrate. The larger beam current and hence count rate can be associated with high accelerating voltages creating a spectral artefact from the Aluminium X-rays. The strong peak at **II** does not appear in the calculated response as shown in figure 4.10 and could be mistaken for contamination from another element. The peak is an artefact known as a *sum peak* [91] which was caused by two Aluminium K-line X-rays reaching the detector within the same capture time. The detector then erroneously recorded the sum of the X-ray energies and hence **II** is the Al+Al sum peak. This effect was observed again at **V** where the Al+Fe sum peak can be seen. A lower count rate minimised the effect. Therefore measurements were conducted with a beam current of 0.8 – 1.2nA whereupon the resulting lower count rate improved the spectral resolution for larger acceleration voltages. This was done by adjusting the electron gun tilt to fine tune the electron flux passing through the mechanical aperture in the SEM.

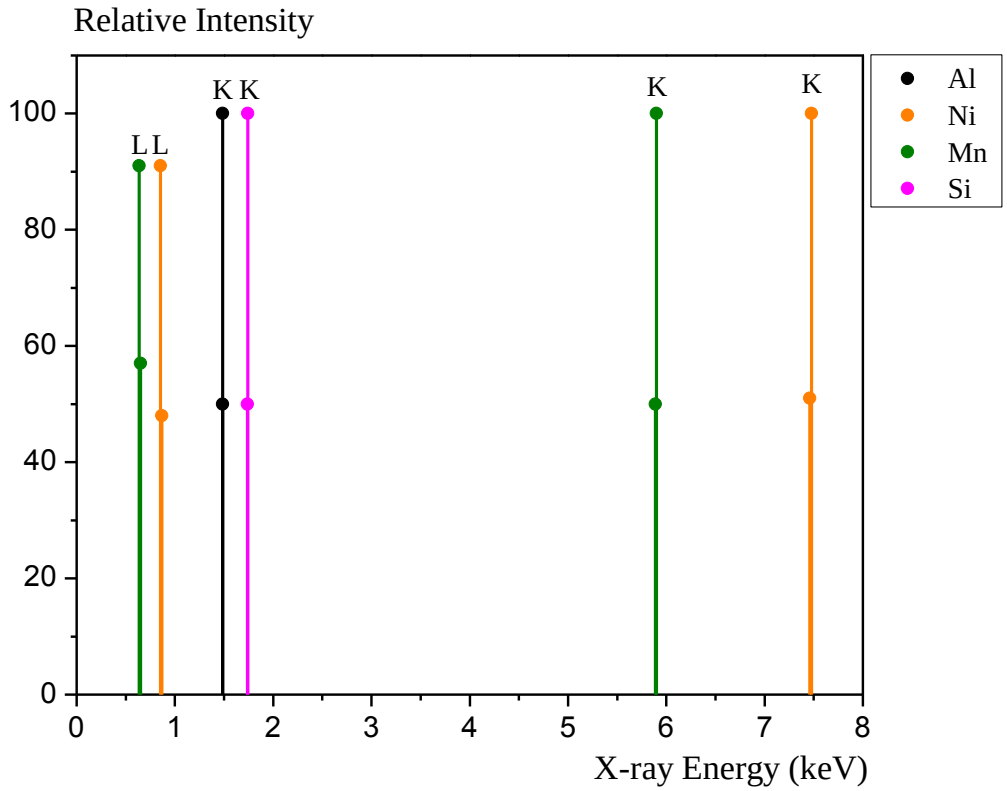

Figure 4.10: The characteristic X-ray energies of Ni_2MnAl on a Si substrate. The intensity is relative to the maximum profile for a characteristic K or L line of each element.

4.3.3 The revised measurement technique

Accurate measurement of the k-ratios of the samples was required to minimise the error in measuring the composition. The bulk standards used by the SEM to generate the k-ratios in the NSS software [102] relied on calibration measurements performed in 2007. The calibration measurements were conducted with unknown beam parameters and therefore could not accurately represent the response of a bulk material under the same conditions as the sample. Calibration stubs were made using high purity (>99.99%) materials cut to a thickness of 0.6mm in order to be level with the thin film samples for easy focusing. The calibration stub made for Fe_2VAl is shown in figure 4.11. The bulk materials were polished using 1µm grain diamond paper in order to match the surface of the samples as well as possible. This was to ensure that there was a similar path of the electrons in the thin film and bulk samples.

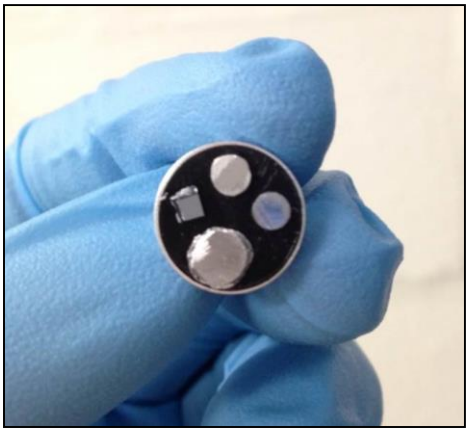

Figure 4.11: The calibration stub developed for Fe_2VAl.

For each measurement the SEM was loaded with a Faraday cup, calibration stub and samples. After selecting the desired accelerating voltage the SEM image was focused on to the edge of a silicon wafer. A magnification of 200x was used to maximise the X-ray yield which corresponded to a measured area of 1800µm^2. The gun tilt was then adjusted until the current was low enough so as not to saturate the detector as indicated by a dead time lower than 50µs on the EDS control software was measured in the Faraday cup. This was to minimise the appearance of sum peaks. The image for each sample was then focused by adjusting the height of the sample stage instead of using the objective lens. This was done to ensure the electron beam conditions were consistent throughout all measurements taken for a particular accelerating voltage. The co-ordinates of each sample were saved to the stage controller which had an accuracy of 0.001mm in the *x*, *y* and *z* directions to ensure the same volumes were being measured across all accelerating voltages. Once each sample was measured the accelerating voltage was then adjusted and the

procedure was repeated until a complete set of data for each sample across a minimum of 5 accelerating voltages in the range of 8keV to 20keV was obtained.

4.3.4 Comparison of STRATAGem and NSS Analysis

The direct comparison of the composition calculated by the STRATAGem and NSS software packages was the final part of the EDS optimisation procedure. It was important that the results were reproducible and agreed with the chemical analysis performed by InterTek as discussed in chapter 3. Both software packages were used to calculate the composition of Fe_2VAl samples under the condition that the sputtering target was doped with increasing amounts of Aluminium between each growth session. This meant that the compositions were verified against the chemical analysis and the expected trend of increasing Aluminium content as doping pegs were added could be tested. If an analysis package was not accurate enough to detect a trend in the Aluminium then it would be considered not accurate enough for the demands of the project. The result of the experiment is shown in figure 4.12. The fitted data results were automatically output in to a table however an example of a fit is shown in figure 3.12 page 46. It should be noted that the Carbon content deposited from SEM beam deposition is not shown in graph.

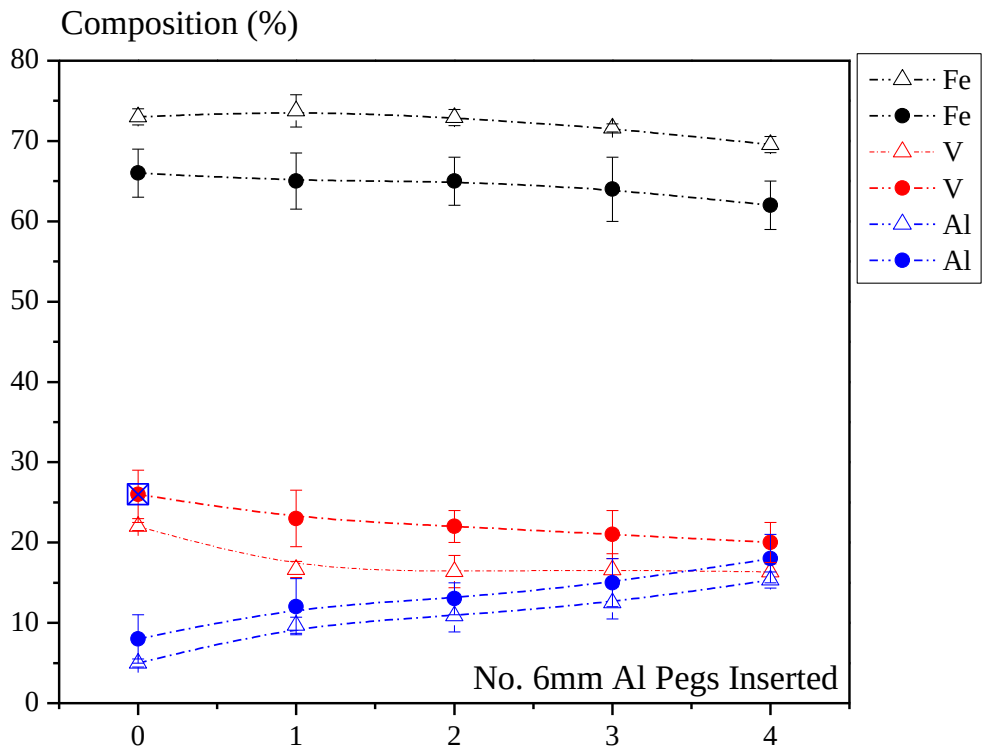

Figure 4.12: Comparison of STRAGAEM (circles), NSS (triangles) and chemical analysis [11] (squares) results taken from the same measurement set.

The STRATAGem and NSS analysis results were recorded for each set of measurements. A different physical model was used to analyse the measured k-ratios. The relatively small error values associated with the NSS data were generated by the software package and are attributed to the quality of fitting to the top of the peaks of the X-ray spectra analysed. The error values associated with STRATAGem are from a combination of five repeat measurements however there will be a systematic error associated with the different surfaces of the bulk and thin film samples. Both analysis techniques follow the same trend of decreasing levels of Iron and Vanadium with an increasing level of Aluminium as expected. The modifications applied by the STRATAGem model for identifying a light element in a heavy element matrix are clear as the Aluminium content is consistently greater but within error of the NSS value. The increase in the Vanadium composition calculated is likely to be a result of measuring the k-ratios manually for STRATAGem. This is because Vanadium and Iron have similar ionising potentials and should have responded similarly under the same beam conditions. The most recent Iron calibrations in the NSS software were within three years of the measurement unlike the Vanadium calibrations which predated the UltraDry detectors installation in the SEM chamber.

The NSS analysis package was convenient to use as it provided a qualitative indication of the sample composition during the measurement procedure. The composition of materials consisting of both light and heavy elements is unlikely to be measured accurately by the NSS package. Therefore the package was limited in its capability for measuring the composition of Heusler alloy thin films. STRATAGem was a more robust analysis technique however its results did not agree within error with the chemical analysis results in table 3.3. Therefore both packages were unsuitable for any application where the composition must be known to within less than 10%. There were some benefits to using EDS to measure composition. For example the stoichiometry of the sample in figure 4.12 was close to Fe_3VAl which lead to the realisation that the Fe_2VAl target was not manufactured correctly. The thickness measurement of the STRATAGem package was also useful for checking the thickness of multilayer thin films if the layers were around 10nm or thicker. EDS was therefore a useful qualitative tool for screening samples however it was not suitable for the high precision required to measure the effect doping the thin films.

4.4 Controlling the Composition of the Heusler Alloy Thin Films

4.4.1 Doping Ni_2MnAl with Transition Metals

The ordering temperature of Ni_2MnAl thin films exceeded 300°C, the maximum temperature for device applications. High temperature annealing is known to cause diffusion between the substrate and Heusler alloy layer which causes the favourable magnetic ordering to be lost [54]. The thin films were doped with Iron and Cobalt in an attempt to substitute Nickel at the X sites in the lattice. Iron and Cobalt were selected because their covalent radii are greater than that of Nickel therefore the lattice should be strained and this should have decreased the Manganese – Manganese nearest neighbour distance to induce antiferromagnetic coupling. Both Fe_2MnAl and Co_2MnAl have been studied and were known to have ordering temperatures lower than the Ni_2MnAl thin films grown in this work [103, 104]. Therefore it was predicted that doping with Iron and Cobalt would also lower the ordering temperature as well as inducing antiferromagnetic order in the films.

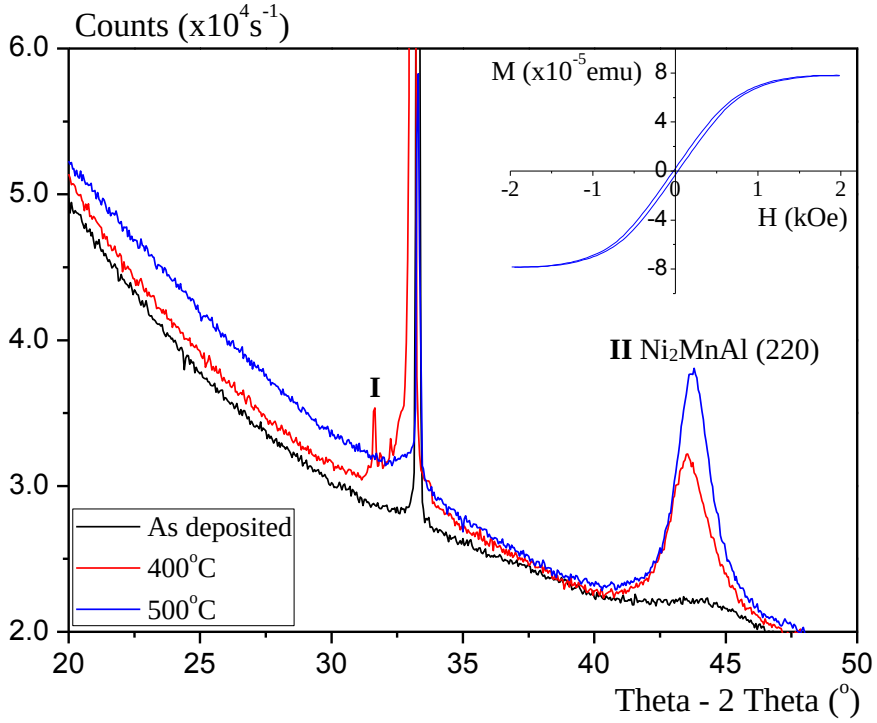

Figure 4.13: Crystallisation of Cobalt doped Ni_2MnAl thin films after two hours of annealing. Inset: a typical hysteresis loop of Cobalt doped Ni_2MnAl annealed for two hours at 500°C.

The $Ni_{2-x}Co_xMnAl$ sputtering targets were doped with one or two Cobalt pegs with a diameter of 6mm. The films exhibited paramagnetic behaviour in the as deposited state. The films successfully crystallised after annealing at temperatures of 400°C and 500°C for two hours as shown in figure 4.13. Both samples exhibited A2 ordering as identified by the (220) peak at **II**.

The peak at **I** for the sample annealed at 400ºC could be mistaken for the Heusler alloy (200) peak which is indicative of B2 ordering. However the sharpness of the profile of the peak suggests that the peak is more likely to be a diffraction fringe that was caused by a slight misalignment of the substrate. This is supported by the broadening of the Silicon substrate (200) peak at 33.2º. The crystallinity was improved when the samples were doped with increasing amounts of Cobalt. The magnetic response of the samples changed from paramagnetic to ferromagnetic after annealing with a magnetic moment of (76.2 ±0.1) μemu measured from the samples with the Q of 1.3 x 10^5. The grains could be $Ni_{2-x}Co_xMnAl$ however the Manganese atoms were not able to couple due to the A2 ordering. A possible alternative is that Co_2MnAl grains had grown because the films were annealed at the ordering temperature of the compound. The samples were annealed for a further two hours and no further crystallisation was observed and the magnetic properties did not change. This could be explained by the presence of Co_2MnAl as the Cobalt content could have been exhausted thus preventing further significant growth of grains.

The $Ni_{2-x}Fe_xMnAl$ sputtering targets were doped with two or four Iron pegs with a diameter of 2mm. The films exhibited ferromagnetic behaviour in the as-deposited state. An average magnetic moment of (1.5 ± 0.1) μemu was measured for four samples grown from sputtering targets doped with two pegs and (2.7 ± 0.1) μemu for four samples grown from sputtering targets doped with four pegs. This was likely due to inhomogeneous regions of higher Iron content being present in the films. The films were then annealed for up to three hours at temperatures of 400ºC and 500ºC however no crystallisation of the Heusler alloy was observed. The average saturation moment of the samples increased to (2.0 ± 0.1) μemu and (3.4 ± 0.1) μemu after annealing at 500ºC for three hours for films grown from sputtering targets that were doped with two and four peg samples respectively. This suggests that crystallisation of an unknown ferromagnetic compound had developed. Attempts to identify the compound were unsuccessful as no X-ray peaks that were not associated with the Silicon substrate were observed.

4.4.2 The Composition of Fe_2VAl films doped with Aluminium

The Fe_2VAl samples that were grown early in the project were measured using EDS and were found to have a very low Aluminium content of ~6%. Therefore the sample stoichiometry was very different to the $Fe_{2.5}V_{0.5}Al$ that was predicted to crystallise as an antiferromagnet [29]. This meant that the composition of the sputtering target was different to the thin films deposited. The composition of the samples was monitored across a period of three months in order to determine whether there was a fault with the sputtering target that caused the composition to change. However the measured composition of the samples remained stable across this period. It was then hypothesised that the Aluminium ions could have been reacting with the local

environment close to the plasma and as a result were not reaching the sample substrates. The sputtering targets were doped with high purity Aluminium pegs in an attempt to achieve the desired composition as shown in figure 4.14.

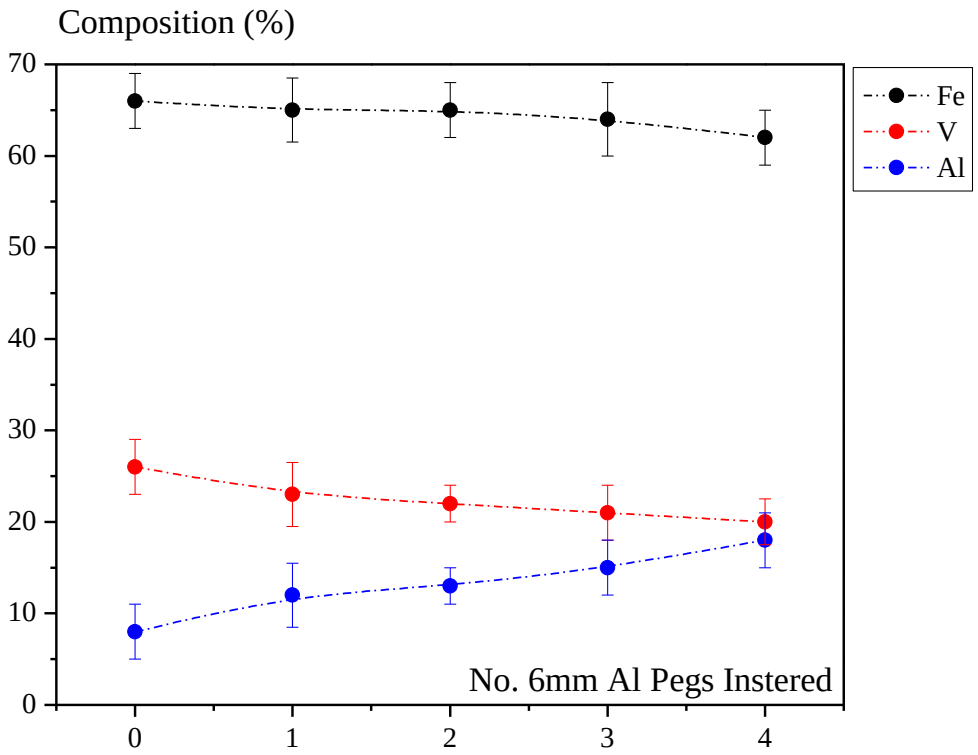

Figure 4.14: Doping Fe_2VAl with 6mm Aluminium pegs.

Extrapolating the Aluminium concentration curve suggests that six Aluminium pegs would be required in the sputtering target to grow samples with a composition of $Fe_{2.5}V_{0.5}Al$ however some Iron doping would also be required. This is because the Vanadium concentration appeared to decline at a sharper rate than the Iron as the samples were doped. The measurements lead to the realisation that the Fe_2VAl target had been manufactured incorrectly as Fe_3VAl. A replacement target with the correct composition was delivered. The films that were grown from the new target were sent to InterTek for chemical analysis as discussed in chapter 3 and were found to contain the desired composition as shown in table 3.3. The process of mapping the crystallisation of Fe_2VAl was repeated for all annealing conditions with samples of the desired composition.

The Ni_2MnAl and Fe_2VAl thin films were successfully crystallised in the A2 phase. It was found that Ni_2MnAl required an annealing temperature of 700°C to crystallise and Fe_2VAl required an annealing temperature between 300°C and 400°C to crystallise. The Ni_2MnAl thin films were grown on a Silver seed layer which improved the crystallisation in the as deposited films. The Ni_2MnAl sputtering target was doped with Cobalt and Iron pegs which improved the

crystallinity of the thin films when annealed at temperatures up to 500ºC. The presence of Nickel, Cobalt or Iron crystallites was indicated in a number of samples by the weak ferromagnetic response of the thin films. A series of bilayers were grown in an attempt to observe any antiferromagnetic behaviour of the selected Heusler compounds through exchange coupling. No exchange coupling was observed which suggested that the crystallinity of the films had to be improved. An optimised experimental procedure for measuring the composition of Heusler alloys using EDS was developed. The EDS measurements failed to agree with chemical analysis which led to the procedure being disused in favour of a comparator measurement.

Chapter 5: Conclusions and Future Work

5.1 Conclusions

The aim of the project was to grow and characterise a selection of polycrystalline Heusler Alloy thin films that could be suitable antiferromagnets for device applications. The work was part of the HARFIR project which aims to find a replacement for the Iridium-based antiferromagnets that are currently being used in the spintronics and magnetic data storage industries [9]. The alloys chosen were Fe_2VAl and Ni_2MnAl because both alloys were constructed of relatively cheap materials and were predicted to be antiferromagnetic following publications from other researchers [29, 41]. The alloys were grown to a thickness of 100nm and were then annealed *ex situ* at temperatures up to 700ºC for up to 6 hours. The Ni_2MnAl samples were then grown by using doped targets on a Silver seed layer as an expansion to the primary objective of the work. The samples were characterised primarily using X-ray diffraction with supporting magnetic and physical measurements that were undertaken using two types of magnetometer and energy dispersive X-ray spectroscopy which had procedure that was optimised for the measurement of Heusler alloys.

The successful crystallisation of A2 phase Ni_2MnAl was achieved by annealing the samples at 700ºC for up to 90 minutes. This was unsuitable for thin film device applications because the extreme annealing temperature meant that the layers in any device would diffuse and rough interfaces would develop. This meant that the properties of devices using Ni_2MnAl could not be controlled easily if they were to be fabricated by the method used in this work. The A2 ordered samples were ferromagnetic and would not be a suitable replacement for Iridium. After 90 minutes of annealing the in-plane X-ray scans indicated that the kinetics of the samples began to favour diffusion between the thin film and the substrate instead of further crystal growth. This could mean that further annealing would not lead to a transition from the A2 phase to a higher degree of order. The B2 phase of Ni_2MnAl was predicted to be antiferromagnetic however it was

not observed in the samples following any of the annealing conditions used. Therefore a combination of the sputtering technique that was used and annealing *ex situ* were found to not be capable of producing antiferromagnetic thin films there are suitable for further work in the HARFIR project. This result led to the investigation of using a seed layer and doped sputtering targets in an attempt to produce suitable Ni_2MnAl films.

The Ni_2MnAl sputtering targets were doped with 6mm diameter pegs that were made of pure Cobalt or 2mm diameter pegs that were made of pure Iron as co-sputtering was not achievable in the HiTUS. The aim was to reduce the ordering temperature of the thin films in order to demonstrate that B2 ordering could be achieved. The samples that were doped with two Cobalt pegs successfully crystallised in the B2 phase after annealing the samples at 500^{o}C for over 3 hours. Both the Cobalt doped and the Iron doped samples were ferromagnetic regardless of the degree of ordering. This was probably the result of local regions within the films that had a higher in concentration of either Cobalt, Nickel or Iron. Alternatively the films could have not been well ordered enough for the Manganese sites to couple antiferromagnetically across the whole sample. The doping of Ni_2MnAl films was promising for improving the crystal quality of the samples with less extreme annealing conditions however the dominant ferromagnetic response indicates that further work will be required for device applications as discussed in section 5.2. The Ni_2MnAl films were grown at a thickness of 20nm on Silver seed layers of thicknesses up to 30nm. A seed layer thickness of 15nm was found to induce the highest degree of ordering within the Ni_2MnAl layer. The films were observed in the A2 phase when deposited on the seed layer however the samples had a ferromagnetic response. Annealing the samples did not cause a transition to the B2 phase which suggested that a seed layer is not entirely sufficient to produce B2 ordered Ni_2MnAl. The Ni_2MnAl samples were readily crystallised in the A2 phase however the desired antiferromagnetic B2 phase was not observed.

The successful A2 crystallisation of Fe_2VAl was achieved by annealing the samples between 300^{o}C and 400^{o}C for up to 6 hours. The Fe_2VAl films exhibited the highest degree of order within the two alloys studied prior to doping the Ni_2MnAl with Cobalt. The films crystallised at annealing temperatures above 400^{o}C however the individual elements segregated from the matrix of the film which lead to a mixture of Heusler alloy grains and pure element grains. There was some evidence to suggest the segregation of Aluminium when the samples were annealed at 400^{o}C however the Heusler alloy grains were far greater in number. This limited the annealing parameters that were suitable good quality films to a small temperature range of 300^{o}C – 350^{o}C. The A2 ordered Fe_2VAl films were ferromagnetic and the moment of the sample increased proportionally to the degree of ordering. This meant that the films were not suitable as an antiferromagnet for the HARFIR project in their undoped condition. Successful fabrication of

potentially antiferromagnetic $Fe_{2.5}V_{0.5}Al$ [29] was not achieved because the Fe_2VAl sputtering target was manufactured incorrectly as Fe_3VAl which resulted in the initial annealing experiments having to be repeated.

The EDS procedure was optimised for the measurement of the composition of Heusler alloy thin films. The aim was to achieve an accuracy of 5% or better in order to detect the change in composition of the films grown by using doped sputtering targets. The electron beam parameters and experimental protocols were optimised which resulted in the reproducible measurement of X-ray spectra for films of a thickness of 20nm or greater. The accuracy of the measurement of the composition of the thin films was tested by comparing the NSS Noran and the STRATAGem analysis packages as part of the investigation. It was found that the STRATAGem package provided the most reliable composition calculations across repeated measurements. Neither package agreed within error with the chemical analysis results as performed by InterTek. This is because both analysis packages underestimated the Aluminium content of the samples as it is difficult to detect a light element in a heavy element matrix when using EDS [90]. Therefore a set of identical thin film calibration samples was produced whereupon the composition was analysed by InterTek. The EDS spectra of the samples were then compared to the calibration samples under identical electron beam conditions in the form of a comparator measurement. This method proved the most useful when having to account for the relatively weak Aluminium response of the samples. The use of EDS proved to be valuable for comparative analysis of the composition of the samples however it was unsuitable for providing absolute data. Other techniques for the measurement of the thin film composition such as X-ray photo spectroscopy could be valuable improvements to EDS however such facilities would have required samples to be sent to collaborators.

The thin films produced were not suitable for device applications by the end of the project. This is because the degree of crystal ordering was not sufficient to have realised an antiferromagnetic state of order in both the Fe_2VAl and Ni_2MnAl compounds. The work has shown that the selected Heusler alloys can be sputtered and annealed to exist in thin film form. The films could be annealed to become successfully ordered in the A2 phase however the results suggest that the energy required to order a lattice from the amorphous state to the A2 state is less than the energy required to transform a lattice from the A2 to B2 state. The use of seed layers and doping were found to be effective techniques for improving the crystallinity of the samples at reduced annealing temperatures. The Ni_2MnAl samples was found to be sensitive to dopants whereupon the magnetic response in the as deposited films changed from being diamagnetic to being ferromagnetic following the addition of Iron or Cobalt to the films. The results are

promising and suggest that further investigation of the selected compounds as potentially antiferromagnetic films would be worthwhile.

5.2 Future work

The successful crystallisation of the selected Ni_2MnAl and Fe_2VAl Heusler alloys demonstrated that such materials can exist as thin films. Therefore the selected alloys are suitable for further investigation in order to try and achieve the antiferromagnetic state of ordering of the films. The conditions of the deposition of the thin films were kept constant in order to control the investigation of how the annealing conditions affected the crystal growth in the films. Parameters such as the bias voltage, sputtering pressure and type of substrate used are all good candidates for optimising the growth parameters of the thin films in a relatively short time scale. Changing the conditions of the deposition of the thin films could change the kinematics of the growth within the crystals leading to deposited films with a higher degree of crystallinity. The HiTUS system was designed as a research tool and therefore would allow a great deal of control in the variation of the sputtering parameters. Another suitable experiment for both Heusler alloys would be to investigate the effects of top or bottom seeding as well as investigating how different capping layers effect the crystallisation of the films. For example Ruthenium could crystallise readily which could seed the growth of crystal grains and a lighter capping layer such as Copper may diffuse differently to the Tantalum capping layer that was used.

The Ni_2MnAl thin films were studied in more detail than the Fe_2VAl because the Fe_2VAl sputtering target was manufactured incorrectly as Fe_3VAl which resulted in a repeat of the annealing experiment. The key aim of any future work in to the investigation of Ni_2MnAl would be to lower the crystallisation temperature in order to realise the B2 phase. A possible future experiment would be to anneal the Ni_2MnAl films with pulses of high energy radiation by using an infrared radiation furnace. If energy input exceeds the relaxation time of diffusion in to the substrate then the Ni_2MnAl may crystallise successfully. Another possible annealing experiment which is possible with the furnace used in this work would be to investigate the rate of heating and the rate of cooling during the annealing procedure. The samples were heated at a rate of 100^oCmin^{-1} however it was possible to have heated the samples at a rate of 1^oCmin^{-1} to 150^oCmin^{-1}. Control of the cooling would require a modification to the setup of the furnace as the temperature controller doesn't allow for the cooling rate to be modified from the environmental conditions of the laboratory. The heating rate could potentially induce a strain in the sample which could be verified by specialised X-ray diffraction scan geometries. The Ni_2MnAl sputtering targets could be doped with Silicon as previous studies have shown that adding Silicon to X_2YAl Heusler alloys increased their crystal quality [8]. The Aluminium and Silicon atoms have similar

bonding radii which may not affect the antiferromagnetic Manganese – Manganese nearest neighbour coupling in the B2 structure.

The Fe_2VAl thin films were found to crystallise at lower temperatures and to a greater degree than the Ni_2MnAl thin films. The key future development for the investigating the predicted antiferromagnetic phase of Fe_2VAl is to adjust the composition of the sputtering target to produce films with the composition $Fe_{2.5}V_{0.5}Al$ as predicted by *Singh and Mazin* [29]. This would lead to an evaluation of the calculations that have predicted the antiferromagnetic state. The trend observed when doping the incorrectly manufactured Fe_3VAl sputtering target with Aluminium pegs could be the ideal method for producing $Fe_{2.5}V_{0.5}Al$ thin films as was discussed in section 4.4.2. Further improvement of the quality of crystallisation of the Fe_2VAl thin films could be achieved by growing the films on top of a Silver seed layer. It is likely that the Fe_2VAl films will crystallise readily in to the A2 phase when deposited as was observed in the Ni_2MnAl thin films.

There are several experiments that can be carried out to further the understanding of how Ni_2MnAl and Fe_2VAl crystallise as thin films. The successful growth of A2 ordered thin films has shown that a higher degree of ordering could potentially be observed if more growth and annealing parameters are studied in detail. The use of a seed layer and doping the sputtering targets has also aided the crystallisation of the thin films and warrants further study. The fabrication of Ni_2MnAl thin films in the B2 phase and the fabrication of $Fe_{2.5}V_{0.5}Al$ thin films in the $L2_1$ phase is essential for testing whether the antiferromagnetic phases of the alloys do exist. If the films can be produced in their antiferromagnetic state then devices consisting of only Heusler alloys forming the active layers could be fabricated. This would demonstrate that Heusler alloys can be used as substitutes for rare metals and other critical materials in devices.

List of Abbreviations

AF	Antiferromagnet
AGFM	Alternating gradient force magnetometer
bcc	Body centred cubic crystal
DC	Direct current
DSP	Digital signal processing
EDX	Energy dispersive X-ray spectroscopy
F	Ferromagnet
fcc	Face centered cubic crystal
FWHM	Full width half maximum
HARFIR	Heusler alloy replacement for Iridium
HiTUS	High target utilisation sputtering
NSS	Thermo Scientific NORAN microanalysis software
RF	Radio frequency
TEM	Transmission electron microscope
VSM	Vibrating sample magnetometer

List of References

[1] N. N. Greenwood and A. Earnshaw, in *Chemistry of the Elements*, Oxford, Butterworth Heinemann, 1991, pp. 1113 - 1143.

[2] R. J. Seymour and J. L. O'Farrelly, Platinum Group Metals, Kirk Othermer Encyclopedia of Chemical Technology, Wiley, 2001.

[3] "Critical Elements pdf," [Online]. Available: http://www.domelatown.nl/uploads/minormetalspdf.pdf. [Accessed 14 August 2014].

[4] Johnson Matthey, [Online]. Available: http://www.matthey.com. [Accessed 8 August 2014].

[5] J. R. Handley, *Plat. Met. Rev.,* vol. 30, pp. 12 - 13, 1986.

[6] H. Stallforth and P. A. Revell, Euromat 99, Materials for Transportation Technology, Munich: Wiley VCH, 2000.

[7] C. Mee and E. Daniel, Magnetic Recording Technology, New York: McGraw-Hill, 1996.

[8] T. Graf, C. Felser and S. S. P. Parkin, *Prog. Solid State Chem.,* vol. 39, pp. 1 - 50, 2011.

[9] N. Mackintosh, "HARFIR," [Online]. Available: http://www.harfir.eu. [Accessed 11 August 2012].

[10] C. P. Bean and H. Jang, *Appl. Supercond.,* vol. 2, p. 689, 1994.

[11] "Intertek," [Online]. Available: http://www.intertek.com/uk/. [Accessed 24 June 2014].

[12] B. D. Cullity and C. D. Graham, Introduction to Magnetic Materials, Hoboken, New Jersey: Wiley, 2009.

[13] W. Z. Heisenberg, *Physik,* vol. 38, pp. 411 - 426, 1926.

[14] R. C. O'Handley, Modern Magnetic Materials: Principles and Applications, Wiley, 1991.

[15] A. H. Morrish and I. M. Society, The Physical Principles of Magnetism, Wiley, 1965.

[16] M. A. Ruderman and C. Kittel, *Physical Review,* vol. 96, pp. 99 - 102, 1954.

[17] T. Kasuya, *Prog. Theor. Phys.,* vol. 16, pp. 45 - 57, 1956.

[18] K. Yosida, *Physical Review,* vol. 106, pp. 893 - 898, 1957.

[19] S. S. P. Parkin, N. More and K. P. Roche, *Physical Review Letters,* vol. 64, pp. 2304 - 2307, 1990.

[20] J. R. Hook and H. E. Hall, Solid State Physics, Chichester: Wiley, 2010.

[21] K. O'Grady, R. Chantrell and I. Sanders, *IEEE Trans. Mag.,* vol. 29, pp. 286 - 291, 1993.

[22] J. Kanamori, *J. Phys. Chem. Solids,* vol. 10, no. 87, 1959.

[23] K. O'Grady, L. E. Fernandez-Outon and G. Vallejo-Fernandez, *J. Magn. Magn. Mater.,* 2009.

[24] F. Heusler, W. Starck and E. Haupt, *Verh DPG,* vol. 5, pp. 220 - 223, 1903.

[25] S. Sakurada and N. Shutoh, *Appl. Phys. Lett.,* vol. 86, pp. 082105 - 8, 2005.

[26] S. Wurmehl, G. H. Fecher, H. C. Kandpal, V. Ksenofontov, C. Felser and H. J. Lin, *Appl. Phys. Lett.,* vol. 88, p. 032503, 2006.

[27] S. Chadov, X. Qi, J. Kubler, G. H. Fecher, C. Felser and S. C. Zhang, *Nat. Mat.,* vol. 9, pp. 541 - 545, 2010.

[28] T. Krenke, E. Duman, M. Acet, E. F. Wassermann, X. Moya, L. Manosa and a. et, *Nat. Mat.,* vol. 4, pp. 450 - 454, 2005.

[29] D. J. Singh and I. Mazin, *Phys. Rev. B.,* vol. 57, no. 14, p. 352, 1998.

[30] R. J. Naumann, Introduction to the Physics and Chemistry of Materials, Boca Raton: CRC Press, 2008.

[31] M. De Graef and M. E. McHenry, Structure of Materials, New York: Cambridge University Press, 2012.

[32] L. R. Fleet, G. Cheglakov, K. Yoshida, V. K. Lazarov, T. Nakayama and A. Hirohata, *J. Phys. D: Applied Physics,* vol. 45, no. 3, pp. 2001 - 2003, 2012.

[33] Carine, [Online]. Available: http://carine.crystallography.pagespro-orange.fr/index.html. [Accessed 01 07 2014].

[34] J. Sagar, L. R. Fleet, M. Walsh, L. Lari, E. D. Boyes, O. Whear, T. Huminiuc, Vick A and A. Hirohata, *Appl. Phys. Lett.,* vol. 105, p. 032401, 2014.

[35] P. J. Webster and K. R. A. Ziebeck, in *Alloys and Compounds of d-Elements with Main Group Elements*, Berlin, Springer, 1988, pp. 75 - 184.

[36] P. J. Webster, K. R. A. Ziebeck and U. N. K, Magnetic Properties of Metals, Springer: Berlin, 2001.

[37] S. Wurhmel, G. H. Fecher, H. C. Kandpal, V. Ksenofontov, C. Felser and H. Lin, *Appl. Phys. Letts.,* vol. 88, p. 032503, 2006.

[38] M. Puselj and Z. Ban, *Croat. Chem. Acta.,* vol. 41, pp. 79 - 83, 1969.

[39] R. A. de Groot, F. M. Mueller, P. G. van Engen and K. H. J. Buschow, *Phys. Rev. Lett.,* vol. 50, 1983.

[40] E. Sasioglu, PhD Thesis, Martin Luther University of Halle-Wittenberg, 2006.

[41] I. Galanakis and E. Sasioglu, *Appl. Phys. Lett.,* vol. 98, p. 102514, 2011.

[42] L. Manosa, A. Planes, M. Acet, E. Duman and E. Wassermann, *J. Appl. Phys.,* vol. 90, no. 10, pp. 8498 - 8500, 2003.

[43] K. R. A. Ziebeck and P. J. Webster, *J. Phys. F: Metal Phys.,* vol. 5, pp. 1756 - 1766, 1975.

[44] F. Gejima, Y. Sutou, R. Kainuma and K. Ishida, *Metall. Mater. Trans.,* vol. 30, p. 2721, 1999.

[45] M. Acet, D. Eyup, E. F. Wassermann, L. Manosa and A. Planes, *J. Appl. Phys.,* vol. 92, no. 7, pp. 3687 - 6392, 2002.

[46] C. Venkatesh, V. Srinivas, V. V. Rao, S. K. Srivastava and P. Sudheer Babu, *J. Alloy. Comp.,* vol. 577, pp. 417 - 425, 2013.

[47] Y. Nishino, M. Kato, S. Asano, K. Soda, M. Hayasaki and U. Mizutani, *Phys. Rev. B,* vol. 79, p. 1909, 2005.

[48] C. S. Lue, H. Joseph, C. F. Ross Jr, C. F. Chang and H. D. Yang, *Phys. Rev. B,* vol. 60, p. 13941, 1999.

[49] E. Popiel, W. Zarek, M. Kapusniak and M. Tuszynski, "Nukleonika," in *S65*, Chlewiska and Siedlce Poland, 2003.

[50] Y. Feng, J. Y. Rhee, T. A. Wiener, D. W. Lynch, B. E. Hubbard, A. J. Sievers, D. L. Schlagel, T. A. Lograsso and L. L. Miller, *Phys. Rev. B,* vol. 63, p. 165109, 2001.

[51] M. Kizilyalli, J. Corish and R. Metselaar, *Pure Appl. Chem,* vol. 71, no. 7, pp. 1307-1325, 1991.

[52] M. Vopsaroiu, M. Gerogieva, P. J. Grundy, M. J. Thwaites and K. O'Grady, *J. Phys. D: Applied Physics,* vol. 38, pp. 490-496, 2005.

[53] M. Vopsaroiu, M. J. Thwaites, S. Rand, P. J. Grundy and K. O'Grady, *IEEE Trans. Mag,* vol. 40, no. 4, pp. 2443-2445, 2004.

[54] J. Sagar, PhD Thesis, The University of York, 2013.

[55] J. Sagar, L. R. Fleet, M. Walsh, L. Lari, E. D. Boyes, O. Whear, T. Huminiuc, Vick A and A. Hirohata, *Submitted to Applied Physics Letters,* 2014.

[56] G. Z. Sauerbrey, *Phys. Verhand.,* vol. 8, p. 193, 1957.

[57] C. Lu and O. Lewis, *J. Appl. Phys.,* vol. 43, p. 4385, 1972.

[58] N. Aley, *PhD Thesis,* The University of York, 2010.

[59] M. von Laue, *Concerning the Detection of X-Ray Interferences,* Nobel Lectures, Physics, 1901-1921.

[60] Rigaku, [Online]. Available: http://www.rigaku.com/products/xrd/smartlab. [Accessed 12 June 2014].

[61] J. Cowley, Diffraction Physics, Amsterdam: Elsevier Science, 1995.

[62] J. Chureemart, P. Chureemart, J. Pressesky, T. Nolan and K. O'Grady, *IEEE Transactions on Magnetics,* vol. 49, no. 7, pp. 3592 - 3596, 2013.

[63] B. D. Cullity and S. R. Stock, Elements of X-Ray Diffraction, Upper Saddle River, New Jersey: Prentice Hall, 2001.

[64] J. Als-Nielsen, Elements of Modern X-Ray Physics, New York: Wiley, 2001.

[65] L. G. Parrat, *Phys. Rev.,* vol. 95, no. 359, 1954.

[66] Rigaku. [Online]. Available: http://www.rigaku.com/service/software/globalfit. [Accessed 19 June 2014].

[67] M. Yasaka, *The Rigaku Journal,* vol. 26, no. 2, 2010.

[68] L. E. Fernandex-Outon, K. O'Grady and M. J. Carey, *J. Appl. Phys.,* vol. 95, p. 6852, 2004.

[69] S. Foner, *Rev. Sci. Instrum,* vol. 30, no. 7, pp. 548-557, 1959.

[70] D. O. Smith, *Rev. Sci. Instrum.,* vol. 27, p. 264, 1956.

[71] Dwight, Menyuk and Smith, *J. Appl. Phys,* vol. 29, p. 491, 1958.

[72] Lakeshore. [Online]. Available: http://www.lakeshore.com/products/Vibrating-Sample-Magnetometer/. [Accessed 4 June 2014].

[73] Microsense. [Online]. Available: http://www.microsense.net/products-vsm.htm. [Accessed 4 June 2014].

[74] J. Mallinson, *J. Appl. Phys.,* vol. 37, p. 2514, 1966.

[75] H. Zijlstra, *Rev. Sci. Instrum.,* vol. 41, p. 1241, 1970.

[76] K. O'Grady, V. G. Lewis and D. P. E. Dickson, *J. Appl. Phys.,* vol. 73, pp. 5608-5616, 1993.

[77] P. Measurements, 4 June 2014. [Online]. Available: http://www.princetonmeasurements.com/agmfeata.htm .

[78] R. Reeves, *J. Appl. Phys. E.,* vol. 5, p. 547, 1972.

[79] W. Roos, K. Hempel, C. Voigt, H. Dederichs and R. Schippan, *Rev. Sci. Instrum.,* vol. 51, pp. 612 - 613, 1980.

[80] J. R. Clemq, *Physica,* vol. 50, p. 153, 1988.

[81] Samx, 04 June 2014. [Online]. Available: http://www.samx.com/microanalysis/products/stratagem_us.html .

[82] M. Ardenne, "Improvements in electron microscopes," Germany, 1937.

[83] M. Ardenne, *Zeitschrift fur physik (translated),* vol. 109, no. 9-10, pp. 553-572, 1938.

[84] M. Ardenne, *Zeitschrift fur Physik (translated),* vol. 19, pp. 407-416, 1938.

[85] J. USA. [Online]. Available: http://www.jeolusa.com. [Accessed 6 June 2014].

[86] Phenom. [Online]. Available: http://www.phenomworld.com. [Accessed 6 June 2014].

[87] A. R. Couture, Université de Sherbrooke, [Online]. Available: http://www.gel.usherbrooke.ca/casino/. [Accessed 2014 06 11].

[88] D. G. Rickerby and J. F. Thiot, *Mikrochimica Acta,* vol. 114, pp. 421 - 429, 1994.

[89] J. L. Pouchou and J. F. Thiot, "Microscopy & Microanalysis," San Fransisco, Bailey and All, 1996, pp. 486-487.

[90] C. R, PhD Thesis, Paris: University of Paris, 1951.

[91] J. Goldstein, in *Scanning Electron Microscopy and X-ray Microanalysis*, New York, Plenum Publishing Corporation, 1984, pp. 222 - 234.

[92] J. A. Small, K. F. Heinrich, D. E. Newbury and R. L. Myklebust, in *SEM*, Illinois, AMF O'Hare, 1979, p. 807.

[93] H. Bethe, *Ann. Phys.,* vol. 5, no. 325, 1930.

[94] SAMx. [Online]. Available: http://www.samx.com/index.html.en. [Accessed 9 June 2014].

[95] H. Yakowitz and D. E. Newbury, in *Ninth Annual Scanning Electron Microscope Symposium*, Chicago, 1976.

[96] J. Goldstein, D. E. Newbury, P. Echlin, D. C. Joy, C. Fiori and E. Lifshin, "Thin Films on Substrates," in *Scanning Electron Microscopy and X-Ray Microanalysis*, New York, Plenum Press, 1981, pp. 354-363.

[97] W. Reuter, in *6th International Conferance on X-Ray Optics and Microanalysis*, Tokyo, 1978.

[98] A. Stefansson, I. Gunnarsson and N. Giroud, *Anal. Chim. Acta,* vol. 582, no. 1, pp. 69 - 74, 2007.

[99] J. M. Mermet, *J. Anal. At. Sprectom.,* vol. 20, pp. 11 - 16, 2005.

[100] A. Montaser and D. W. Golightly, Inductively Coupled Plasmas in Analytical Atomic Spectrometry, New York: VCH Publishers, 1988.

[101] K. O'Grady, L. E. Fernandez-Outon and G. Vallego-Fernandez, *J. Mag. Mag. Matr.,* vol. 322, pp. 883 - 899, 2010.

[102] T. Scientific. [Online]. Available: http://www.thermoscientific.com/en/product/noran-system-7-x-ray-microanalysis-system.html. [Accessed 14 August 2014].

[103] Z. Liu, X. Ma, F. Meng and G. Wu, *J. Alloy Compd.,* vol. 509, no. 7, pp. 3219 - 3222, 2011.

[104] M. Yin, S. Chen and P. Nash, *J. Alloy Compd.,* vol. 577, pp. 49 - 56, 2013.

[105] C. Hellier, Handbook of Nondestructive Evaluation, McGraw Hill Professional, 2001.

[106] I. Galanakis and E. Alou, *Applied Physics Letters,* vol. 98, 2011.